VOLCANIC, STRUCTURAL, AND MORPHOLOGICAL
HISTORY OF SANTA CRUZ ISLAND,
GALÁPAGOS ARCHIPELAGO

A Thesis

Presented in Partial Fulfillment of the Requirements for the

Degree of Master of Science

with a

Major in Geology

in the

College of Graduate Studies

University of Idaho

by
Darin Schwartz
December 2014

Major Professors: Karen S. Harpp, Ph.D. and Mickey E. Gunter, Ph.D.

Authorization To Submit Thesis

This thesis of Darin Schwartz, submitted for the degree of Masters of Science with a major in Geology and titled " Volcanic, Structural, And Morphological History Of Santa Cruz Island, Galápagos Archipelago" has been reviewed in final form. Permission, as indicated by the signatures and dates given below, is now granted to submit final copies to the College of Graduate Studies for approval.

Co-Major Professors: _____ Date: _____

        Karen S. Harpp, Ph.D.

        _____ Date: _____

        Mickey E. Gunter, Ph.D.

Committee
Members: _____ Date: _____

        Eric Mittelstaedt, Ph.D.

        _____ Date: _____

        William M. Phillips, Ph.D.

Department
Administrator: _____ Date: _____

        Mickey E. Gunter, Ph.D.

Discipline's
College Dean: _____ Date: _____

        Paul Joyce, Ph.D.

Final Approval and Acceptance
Dean of the College
of Graduate Studies: _____ Date: _____

        Jie Chen, Ph.D.

Abstract

Santa Cruz Island is one of the oldest volcanoes in the Galápagos Archipelago; little is known about its history or its evolutionary relationship to the younger western shield volcanoes. Of particular note, the island's northern and southern flanks are deformed by a series of major normal faults of unknown origin. Using an array of multidisciplinary tools, including field mapping, global positioning satellite measurements, gravity measurements, $^{40}Ar/^{39}Ar$ geochronology, and ^{3}He exposure dating, I construct a structural and volcanic history of Santa Cruz. The $^{40}Ar/^{39}Ar$ ages reveal that since ~1.5 Ma, the island has experienced two phases of volcanism, separated by ~400 ky. The first occurred from 1620 ± 15 to 1160 ± 35 ka (1σ); the second lasted from 699 ± 45 to 74 ± 19 ka. Volcanism during the second phase was focused along an E-W trending summit vent system, from which all lavas erupted <200 ka were deposited on the southern flank. Structural observations suggest that the island has experienced two major faulting episodes. North flank faults formed after 1160 ± 35 ka, whereas the Southern Faults were initiated between 274 ± 18 and 38 ± 8 ka. Gravity results indicate two E-W trending, intrusive complexes; one is centered north of the island's summit and the other is beneath the southern flank. When integrated, our data are consistent with a model wherein the Northern Faults are associated with regional uplift occurring after 780 ka and before 500 ka (Bow, 1979). This deformation event may be related to establishment of the summit vent system and the initiation of the second phase of volcanism. The second volcanism phase is contemporaneous with the formation of the Southern Faults. Southward spreading along the island's southern flank accommodated extension initiated by intrusions, which ceased with volcanism ~30 ka. The extended volcanic activity characteristic of Santa Cruz and of other older Galápagos Islands may be the result of rejuvenated volcanism linked to regional uplift event(s); low volume eruptive fluxes during extended activity downstream of the plume center may explain the morphological differences observed between eastern and western volcanoes in the archipelago.

Acknowledgements

Table of Contents

List of Figures

List of Tables

Chapter 1: Introduction

1.1. Ocean Island Morphology and Evolution

The morphology of a volcanic island within any hotspot-generated archipelago is a product of the volcanic activity contributing to its construction as well as the deformational and erosional processes leading to its destruction. The relative balance between these two influences changes with time and leads to morphological variations of islands within archipelagos.

Of all the hotspot-derived island chains, the Galápagos Archipelago exhibits some of the most extreme morphological differences between its young and old volcanoes (e.g., McBirney and Williams, 1969; Figs. 1, 2). In contrast to other large island chains, however, Galápagos volcanoes have experienced limited erosion owing to the low annual rainfall (Grant and Boag, 1980). There is also little evidence for large scale mass wasting, even on the oldest islands (e.g., Bow, 1979; Chadwick and Howard, 1991; Geist et al., 1986; Swanson et al., 1974). Despite the lack of erosion, volcanoes along the central hotspot track vary considerably from west to east in terms of their morphology (Fig. 2; McBirney and Williams, 1969; White et al., 1993). Younger volcanoes in the west (Fernandina, Isabela) are tall structures (e.g., Fernandina's summit reaches 1500 m) with large summit calderas (Fig. 2). Older, eastern islands (Santiago, Santa Cruz, San Cristobal) are shorter and are characterized by linear summit vent systems without calderas (e.g., Swanson et al., 1974). Little is known about the evolutionary relationship between the older eastern islands and their younger western counterparts.

In addition, the period of active volcanism in the Galápagos extends beyond what is predicted on the basis of the traditional hotspot theory (Morgan, 1972). In Hawaii, shield stage volcanism ends ~100 km downstream of the plume center (e.g., Garcia et al., 2010). When taking the slower plate motion in the Galápagos into account (51 km/Ma, compared to 72 km/My in Hawaii; Argus et al., 2011), volcanism is relatively extended in comparison to Hawaiian volcanoes. In the Galápagos, intermittent shield stage volcanism continues for up to 200 km beyond the presumed plume center, located near Fernandina Island (e.g., White et al., 1993).

In this study, I address two fundamental questions pertaining to eastern Galápagos volcanoes: (1) What is the cause of the morphological contrast between eastern and western volcanoes in the Galápagos; and (2) Why does volcanism in the eastern Galápagos extend beyond the ~100 km range expected for primary volcanism in hotspot systems, as scaled to the plate velocities in the Galápagos from what is observed in Hawaii (e.g., Garcia et al., 2010)?

Santa Cruz Island, located in the central Galápagos Archipelago (Figs. 1, 3), is ideal for investigating the link between eastern and western volcanoes. The island has a long history of volcanism exposed (e.g., Bow, 1979), which may record the transition from a caldera forming eruptive style. Santa Cruz Island is a shield volcano, lacking a caldera which typifies the eastern Galápagos volcano morphology. Furthermore, Santa Cruz Island has more than 1 My of volcanic stratigraphy exposed (White et al., 1993). The exceptional exposure allowed us to sample much of the recent history of the volcano. The island is visibly deformed by a series of normal faults on its northern and southern flanks (Fig. 3). Although most of the eastern islands are deformed by normal faults (Santa Cruz, Santa Fe, San Cristobal; Swanson et al., 1974; Bow, 1979), the faults are best exposed on Santa Cruz. Because these fault systems only occur on the older, eastern volcanoes, they may provide crucial insight into the morphological evolution of Galápagos volcanoes.

We construct a quantitative history of volcanism and deformation on Santa Cruz Island using a multidisciplinary dataset. Combining $^{40}Ar/^{39}Ar$ geochronology of lavas, ^{3}He exposure dating of faults, field mapping, and a gravity survey of the island, I propose a comprehensive model describing the magmatic and morphological evolution of the island and of the Galápagos Archipelago.

1.2. Geologic Background

1.2.1. The Galápagos Archipelago

The Galápagos Archipelago is a plume-sourced island chain that rests upon a shallow ESE-trending basaltic platform on the Nazca Plate (Fig.1). The center of the archipelago is approximately ~300 km south of the Galápagos Spreading Center and ~1000 km west of

Ecuador. The Galápagos consists of 10 major islands composed of basaltic shield volcanoes, as well as numerous minor islands and seamounts (McBirney and Williams, 1969), all generated by the Galápagos mantle plume (Fig. 1; e.g., Morgan, 1972). The westernmost island of Fernandina is the most active volcano in the archipelago (e.g., Kurz et al., 2014), erupting lavas with $^3He/^4He_i$ up to 27 R_a (Graham et al., 1993; Kurz and Geist, 1999; Kurz et al., 2009). It is presumably at or near the present day center of plume upwelling. As the islands drift from the hotspot source, they subside, resulting in their eventual submergence ~5 My after their initial formation over the hotspot center (Geist et al., 2014a).

1.2.1.2 Western Galápagos Volcanoes

In the Galápagos Archipelago, volcanoes are characterized by a morphologic dichotomy between east and west (Fig. 2). The western islands (Fernandina, Isabela) are built of tall (>1500 m) shields with broad, flat tops, steep upper slopes, and summit calderas (McBirney and Williams, 1969; White et al., 1993). McBirney and Williams (1969) describe the western shield volcanoes as "overturned soup plates", which contrasts with the "overturned saucer" shape that typifies shield volcano morphologies in other island chains (e.g., Hawaii). All western Galápagos volcanoes have both radial and circumferential vent patterns (McBirney and Williams, 1969; Nordlie, 1973; Mouginis-Mark et al., 1996; Chadwick and Howard, 1991). The characteristic "overturned soup plate" morphology of the western Galápagos has been attributed to variations in effusion rates at the volcanoes' vent systems (Chadwick and Howard, 1991). High effusion rates and low viscosity lavas erupted from radial fissures on the islands' flanks lead to large, relatively flat bases (Naumann and Geist, 2000). Eruptions from circumferential fissures (which are presumably initiated following caldera collapse; Naumann and Geist, 2000) are less voluminous, have higher viscosities, and result in steeper summit slopes (Chadwick and Howard, 1991).

A three-stage model for the evolution of western Galápagos volcanoes has been proposed on the basis of their position relative to the plume center (Geist et al., 2014b). The first is called the Juvenile Transient Phase and occurs prior to the volcano reaching the hotspot. During the Juvenile Transient Phase, magmas begin to form under incipient thermal and chemical influence of the plume. Once directly over the plume, the volcano enters its second stage and becomes mature (e.g., Fernandina) and is in the Mature Steady-State Phase.

During the mature phase, a crystal mush zone that has formed beneath the volcano buffers magma to relatively homogeneous compositions and a sill-like magma chamber forms beneath the volcanic edifice (e.g., Fernandina Island). As the volcano drifts further from the plume, the mush zone cools and fractionates to become more felsic, which erupts in the final Dying Cooling Phase of the volcano (e.g., Alcedo Volcano, Isabela Island). In this evolutionary model, Geist et al. (2014b) only consider Alcedo and younger volcanoes in the western archipelago, but none of the older islands in the east.

1.2.1.1. Eastern Galápagos Volcanoes and Santa Cruz Island

In the eastern Galápagos Archipelago (Figs. 1, 2), there is a distinct absence of calderas. Here, linear monogenetic cone fields form summit vent systems, and, where present, faults are sub-parallel to vent orientation (e.g., Swanson et al., 1974; Bow, 1979; Geist et al., 1986; Pryet et al., 2012). The distribution and orientation of eruptive vents documented in the eastern Galápagos, (e.g., Santiago, Santa Cruz, San Cristobal) is more akin to that of other archipelagos (e.g., Hawaii and the Canary Islands) than it is to the western Galápagos edifices. In Hawaii, for example, eruptive fissures and vents are predominantly oriented parallel with each other along a primary rift zone (e.g., Fiske and Jackson, 1972; Carracedo et al., 2010).

The location of Santa Cruz Island is in the approximate center of the Galápagos Archipelago, ~130 km east of the present day plume center (e.g., Kurz and Geist, 1999; Fig. 1). Santa Cruz Island is the most populous island in the Galápagos, with roughly 12,000 residents, the majority of whom live in the town of Puerto Ayora on the southern flank of the volcano. Magmatic activity on Santa Cruz Island has been documented using K/Ar and $^3He/^4He_c$ surface exposure dating; ~20 dated samples indicate that volcanic activity on the island lasted for over a million years (Cox and Dalrymple, 1966; Bailey, 1976; Bow, 1979; White et al., 1993; Kurz and Geist, 1999). Geist et al. (2014a) evaluated and compiled all reliable ages for Santa Cruz Island (5 samples) and cites 1.12 ± 0.07 ka as the oldest age for the island (Geist et al., 2014a; White et al., 1993). Older eruptive ages have been recorded on the volcano, extending up to 2.2 Ma; these dates (Cox and Dalrymple, 1966; Bailey, 1976; Bow, 1979), however, are not considered reliable owing to their large analytical uncertainties (Geist et al., 2014b). The youngest recorded volcanism is observed on the island's southern flank, with an age of 24 ± 11 ka (White et al., 1993).

Two chemically distinct phases of volcanism denoted as the Platform Series and the Shield Series (Bow, 1979) punctuate the volcanic stratigraphy of Santa Cruz Island. As Santa Cruz Island was transported from its hotspot source, waning influence of the Galápagos mantle plume lead to compositional variation in the Platform and Shield Series lavas (Wilson, 2013). The Platform Series is comprised of basalts ranging between tholeiites and ferrobasalts (Bow, 1979; Wilson, 2013). Reversely polaritylavas, erupted prior to 781 ka (Bow, 1979; Singer and Pringle, 1996) make up the entirety of the Platform Series. Homogeneous lavas and evidence for shallow fractionation (1-4 kbar) indicate the presence of a relatively high-volume, long-lived, shallow crustal magma chamber (Wilson, 2013).

The younger Shield Series is composed of alkali basalts and hawaiites (Bow, 1979; Wilson, 2014). All Shield Series lavas are normal polarity, having erupted during the Brunhes from 779 ka to the present (Bow, 1979; Singer and Pringle, 1996). In contrast to the more homogeneous Platform Series, the greater chemical heterogeneity of the Shield Series lavas indicates that magmas were not homogenized in a central magma chamber (Wilson, 2013). Furthermore, the majority of Shield Series lavas were fractionated at pressures 2 to 3 times deeper (4-6 kbar) than those of the Platform Series. Wilson (2013) attributes the lack of a robust magma chamber during the Shield Series phase to the waning influence of the Galápagos mantle plume as Santa Cruz Island drifted eastward, resulting in decreased melt generation and supply rates (Wilson, 2013).

Santa Cruz and the other eastern islands in the archipelago have experienced volcanic activity that extends significantly beyond what is predicted for the evolution of western Galápagos volcanoes (White et al., 1993; Geist et al., 2014b). According to the evolutionary model proposed by Geist et al. (2014b), the eruption of late-stage, felsic volcanic products should occur by ~50 km from the hotspot center (i.e., the present-day location of Alcedo volcano), reflecting a rapid shutdown of its magmatic system. On Santa Cruz, however, basaltic volcanism continues for >1 My past the predicted shift to felsic volcanism (Bow, 1979; Kurz and Geist, 1999). Wilson (2013) proposes that volcanism continues beyond the proposed termination of western Galápagos activity in a Gradual Dying Phase, which

replaces the Geist et al. (2014b) Dying Cooling Phase, represented by Alcedo Volcano. She attributes the presence of the Gradual Dying Phase to the fact that eastern volcanoes are underlain by younger, thinner, hotter lithosphere than the young western shields, allowing the eruption of smaller melt volumes after the solidification of the shallow magma chamber (Wilson, 2013).

Chapter 2: Methods

2.1 Structural Geology

We identified and mapped structural lineaments on Santa Cruz Island utilizing a combination of aerial photographs, Google Earth satellite imagery, and a digital elevation model (d'Ozouville et al., 2008a) (Figs. 3, 4). The primary measurements collected from the digital imagery were lengths and orientations of structural lineaments. Types of lineaments documented include faults, fissures, monoclinal folds, and the alignment of elongate pit craters as well as any prominent regional structures (Fig. 5). Orientation statistics that I calculated from these data were weighted by fault length. This was done to prevent a bias due to limitations of imagery, which sometimes resulted in 'artifact' segmentation. Throw along faults was also recorded at 500 m intervals along all structures exhibiting displacements greater than the resolution of our DEM (~5 m). I distinguished pit craters from volcanic vents by the absence of a raised rim of erupted material around the central crater. From the locations and sizes of the mapped vents we calculated a surface area weighted directional distribution using ArcGIS.

In the field, structural analysis was focused in the northeast and south-central parts of Santa Cruz Island (Fig. 3), in part because the southern flank and the central highlands of Santa Cruz Island are obscured by thick vegetation and are virtually inaccessible. Consequently, field investigations in locations other than the northeastern flank of the island (which is the dry side of the island) were limited to the area around the town of Puerto Ayora, as well as along roads, game trails, and shorelines. I documented total fault throw using post-processed kinematic elevation data collected with a Trimble R7 GPS system. The GPS measurements were primarily used to validate total throw measurements from the digital elevation model (Fig. 6, Table 1). Other field data include fault length and throw (Figs. 3, 6, 7), as well as fissure dilation.

2.2. Geochronology

2.2.1. ^{40}Ar/^{39}Ar Dating

Samples were collected from 15 basaltic lava flows, which, on the basis of field evidence, are believed to be representative of the island's volcanic history, insofar as it is exposed and accessible. Attention was taken to sample localities where ages of lavas could be used to constrain the timing of deformation on the island. Wilson (2013) analyzed all samples for major and trace elements as well as Sr, Nd, and Pb isotopic ratios.

Samples for $^{40}Ar/^{39}Ar$ analysis were crushed and milled using a mechanical jaw crusher and disk pulverizer, sieved to 850-1000 μm, and cleared of phenocrysts under a binocular microscope, leaving only microcrystalline groundmass. Picked groundmass from each sample was cleaned, irradiated, and analyzed at Oregon State University. Approximately 200 days after irradiation, samples were incrementally heated to release argon. Gas released during step heating was analyzed using the ARGUS VI multi-collector noble gas mass spectrometer following the methods described by Sinton et al. (1996) and references therein. The incremental heating steps creating a plateau in $^{40}Ar/^{39}Ar$ were averaged to produce an age for each sample (Fig. 8). The plateau age average was inversely weighted according to the analytical uncertainty of each step. The amount of Ar released (% Ar) and the number of heating steps (N) used to calculate each age were also recorded (Table 2). A linear regression was calculated for the steps used in the calculation of the plateau age using an inverse isochron ($^{36}Ar/^{40}Ar$ versus $^{39}Ar/^{40}Ar$), wherein the age of the sample is derived from the slope and the initial $^{36}Ar/^{40}Ar$ is calculated from the inverse of the y-intercept (Fig. 8). Samples that yielded ages with negative or discordant plateaus and isochron ages are considered unreliable and are not included in the discussion (Fig. 9).

2.2.2. Surface Exposure Dating

2.2.2.1. Field Measurements and Sample Collection

The primary goal of the geochronological exposure study is to constrain the timing of fault and fissure formation on the southern flank of Santa Cruz Island. Therefore, the procedure described below was followed to ensure that the exposure age of the sample would reflect the minimum age of the fissure-forming event related to each sample. I collected all samples from basaltic lava flows, within the vertical fissure that breaches the upper hinge of deformational monocline structures. Sample locations were dictated primarily by the

presence of modal olivine in places where material could be retrieved using a hammer and chisel. Furthermore, samples were removed from the fissure walls as low in the volcanic stratigraphy and as far from adjacent surfaces as possible. Sites were selected where I could match joint patterns on adjacent fissure walls, indicating that no significant erosion of the wall had taken place since the deformation event. Where I could not meet the aforementioned conditions, I chose sites that exhibited minimal evidence of erosion, including limited talus at the base of the fissures and abundant lichen on fissure walls. In these cases, cosmogenic ages represent a minimum age for the formation of the fissures. A similar approach to sampling the scarp face offsetting basaltic lavas has been adopted elsewhere (Mackey et al., 2014).

At each sample site, topographic shielding measurements were made using a Brunton compass and handheld Suunto PM-5/360 clinometer. I measured horizon angle and azimuth at intervals of 30° and wherever abrupt deviations in horizon angle occurred. Vegetation coverage was also noted but was not used in the final age calculations. Corrections for the production of ^{3}He as a function of this shielding were calculated using the methodology of Balco et al. (2008), assuming complete attenuation of cosmic rays for all geometric and topographic shielding.

Cosmogenic dating samples were squared using a rock saw and cut to a thickness between 2 and 3 cm. The pieces were crushed and milled using a mechanical jaw crusher and disk pulverizer, then sieved to between 250 and 1200 µm. I removed magnetic groundmass with a hand magnet and Frantz magnetic separator. Olivine grains were then handpicked under a binocular microscope, typically from the 500-850 µm, non-magnetic sieve fraction.

The olivine was crushed and melted at Woods Hole Oceanographic Institute (WHOI) to permit helium extraction and measurement. Crushing the sample releases the He contained primarily in melt and fluid inclusions, which is representative of the inherited component and measured as ^{3}He/^{4}He (Kurz, 1986a). Melting the crushed fraction in a single step releases the remaining gas, yielding total concentrations of ^{3}He and ^{4}He. I assume that the inherited He ratio does not change due to the radiogenic production of ^{4}He from the decay of Th and U. This assumption is valid due to the low concentration of U and Th in the samples (<1ppm; Wilson, 2013) and their youth. Since the cosmogenic production of ^{4}He is insignificant

compared to that of ^{3}He (Kurz, 1986b), the cosmogenic component of ^{3}He can be calculated using the following two equations:

$$^3He_i = {}^4He_t \times ({}^3He/{}^4He)_i \qquad (Eq.\ 1)$$

$$^3He_c = {}^3He_t - {}^3He_i \qquad (Eq.\ 2)$$

where c, t, and i represent concentrations of cosmogenic, total, and inherited helium, respectively.

The samples were analyzed using the rock analysis mass spectrometer system (MS2) at WHOI, consisting of a 90$^°$ magnetic sector noble gas mass spectrometer and a quadrupole mass spectrometer. I carried out the analyses following the analytical procedure described by Kurz and Geist (1999), Kurz (1986b), and Kurz et al. (1996) (Table 3).

We conducted duplicate analyses to determine analytical reproducibility (Table 3, Fig. 10). The relative differences between each pair of replicate analyses are 12%, 2.5%, and 0.059%. The analytical precision ranges from 2.5-35% (1σ).

2.2.2.2. Cosmogenic Age Calculations

For each sample, the cosmogenic ^{3}He concentration was determined using a combination of Equations 1 and 2. I calculated an exposure age for each sample (Table 4) using the cosmogenic ^{3}He concentration from the samples. For age calculations, I used a sea level-high latitude ^{3}He production rate in olivine of 121 atoms g^{-1}yr^{-1} (Goehring et al., 2010), scaled to the appropriate latitude and elevation of each sample site using the relationship of Lal (1991) as modified by Stone (2000). Given that all samples were collected on surfaces with a dip greater than 30°, a final scaling factor for the production rate incorporating surface dip and sample thickness was calculated using the equations derived by Dunne et al. (1999) and modified by the measured topographic shielding (Balco et al., 2008).

Two uncertainty measurements are calculated and plotted for each analysis (Table 4, Fig. 11). The first (and smaller) uncertainty is produced from only analytical uncertainty. I determined the second, larger uncertainty, by taking into account the production rate

uncertainty and scaling factors presented in Goehring et al. (2010), summed in quadrature with the analytical uncertainty. The ages and uncertainties for replicate analyses are averaged in the final age plot (Fig. 11) for each sampling site. In addition to the age calculation described above, a second age has been calculated omitting the shielding correction (Table 4, Fig. 11). By not including shielding, the latter age should be interpreted as a gross minimum for each sample and is used to evaluate the accuracy of the shielding correction on the age calculation.

Since fault segments are >1 km in length along a single fault (Fig. 7), I assume that samples collected on the same fault should yield the same age when sampled within ~1 km along strike to one another. Therefore, for samples that meet this criterion, I calculate a mean age for the fault from which they were collected (Fig. 11); ages were weighted according to their analytical uncertainty.

2.3. Gravity

2.3.1. Gravity Measurements

A gravity survey was conducted by myself and two other individuals, in a series of four transects, radiating from a central base station near the town of Santa Rosa (Fig. 3). Measurements were taken at 1 km intervals using a model G LaCoste and Romberg gravity meter. We collected a total of sixty-five measurements during the 28-hour survey. Before and after completing each of the four survey legs, we measured gravity at the central base station. We made all measurements on the side of the main road. At each measurement location, we leveled the gravimeter by hand, and recorded the latitude, longitude, and elevation using a Trimble R7 GPS system. In addition we recorded the time, internal temperature of the gravity meter, battery voltage, and gravity reading at each site (Table 5).

The gravity measurements were reduced to a Free Air Anomaly (FAA) by removing instrumental drift between base station measurements (~0.01 mGal), and by removing the effect of elevation and the WGS-84 reference ellipsoid (Table 5, Fig. 12). Final Bouguer gravity anomaly (BA) results (Table 5, Fig. 13) were calculated by subtracting the effects of the mass of Santa Cruz and Baltra Islands at each survey point. I represent the mass of the

two islands as a matrix of 30 x 30 meter-wide prisms with height taken from the DEM (d'Ozouville et al., 2008b), all with densities of 2400 kg/m^3. On the basis of five BA anomalies calculated using island densities between 2000 and 2800 kg/m^3, the intermediate value of 2400 kg/m^3 produced a BA anomaly least correlative to elevation (Fig. 14); thus, 2400 kg/m^3 was chosen as the best fit for the island's mean density (Fig. 13). For the BA calculation, the effect of each prism was removed from the gravity survey points according to the methods of Mittelstaedt et al. (2014) (Table 5). Relative accuracy on the order of 0.01 mGal (1σ, Table 5) in the calculated BA is represented by variation in the replicate measurements at the base station after I applied all corrections.

2.3.2. Gravity Inversion

The purpose of the gravity inversion was to constrain the approximate width and density of the source responsible for the measured gravity anomalies on Santa Cruz Island. Final density anomalies (measured as kg/m^3 relative to the assumed density of 2400 kg/m^3) were obtained by inverting the final BA calculated from the measured gravity data. I split the dataset into an E-W and a N-S transect before performing the inversion on the gravity data. For both transects, a row of prisms was created to replicate the calculated BA from the data. Each prism has a width of 1700 m in the transect-parallel direction. Individual prisms are 10^9 m long normal to the transect orientation, meant to represent infinitely long prisms. For each inversion run, I vary the depth below the ground to the top of the prism (d) and prism thickness (t) to determine the best fit to the BA data. The BA for each measurement point along both transects was inverted for $\Delta\rho$ (density variation) using a least squares method (Mittelstaedt et al., 2014).

We generated six inversion scenarios; each inversion has specified values for depth to the upper prism surface and thickness of the prism layer (Fig. 15). For the six inversions, I varied the prism thickness between 0.5 to 2 km at 500 m intervals, and depth to the top of the prism layer was changed between 0 and 1 km, again at 500 m intervals.

Chapter 3: Results

3.1. Structural Geology

I have prepared a structural geology map of Santa Cruz Island that incorporates existing digital and field data (Fig. 3). I have divided the structures on Santa Cruz Island into two categories, made on the basis of their morphology and their location on the island. In general, faults on the northeastern flank of Santa Cruz Island (Fig. 3) are less intact and have throws that increase shoreward; these are referred to hereafter as the Northern Faults. In contrast, faults in the south central sector of the island (Fig. 3) are more intact, displaying throws that exhibit no correlation with proximity to the shore; this group I refer to as the Southern Faults. There are, however, small sets of faults on the northwest and southwest flanks of Santa Cruz Island that are isolated from the two primary fault groups. These isolated faults have been included in the Southern Fault group because they exhibit similar structural characteristics in the satellite imagery.

3.1.1. The Northern Faults

The faults on the northern flank of Santa Cruz Island are concentrated along the shoreline (Figs. 3, 4). Seymour (< 1 km north of Baltra), Baltra, and Santa Fe Islands have faults with similar morphology, which I observed in satellite imagery and the DEM. The Northern Fault group has a length-weighted mean orientation of 079° and a corresponding principal mode orientation of approximately 075° (Fig. 5). Characteristically, the Northern Faults have vertical scarps and large piles of rubble at their bases; in places, only a steep rubble pile separates the footwall and hanging wall surfaces, with no exposed scarp face (Fig. 16). The Northern Faults are oriented approximately WSW-ENE. They occur as both north- and south-facing structures, forming narrow grabens that can be identified by geometric indentations along the shoreline of the island. Along most faults on the northeastern flank of Santa Cruz Island, throw increases from west to east. In other words I observe the maximum throw for the Northern Faults along the east coast of the island (Figs. 3, 4). The maximum throw measured along the Northern Faults is 52 m (Fig. 3). In places, undeformed lavas are seen abutting the fault scarps. All Northern Faults extend no more than 5 km from

the shoreline. Since fault throw is nonzero at the shoreline, I assume that the faults extend beneath the ocean, making our fault lengths minimum estimates.

3.1.2. Southern Faults

Faults within the Southern group are distributed primarily across the south-central flank of Santa Cruz Island (Fig. 4A). The Southern Faults have a length-weighted mean orientation of 088° and a principal mode orientation of 115° (Fig. 5). Vertical fissures, trending approximately W-E, commonly breach narrow monoclinal folds, a characteristic of the Southern Fault group. The nearly vertical faults on the southern part of the island accommodate both vertical and horizontal displacement. The result of this combined offset is a gaping fissure that separates an up-thrown and a down-thrown block. The depth of the fissure is variable depending on the amount of rubble that has filled in the gap. Furthermore, a more shallowly dipping frictional normal fault plane at depth is never observed at the vertical fault scarp's base. The location of the hanging-wall block relative to the footwall block alternates north and south of the breach, suggesting that in the subsurface, the fault dips are not preferentially directed toward the center of the island or the northern coastline.

The mapped faults appear in satellite imagery as relatively short, aligned segments. In some cases, however, faults that appear to be segmented in the satellite imagery were observed to be continuous features in the field. Nevertheless, throw measurements along single fault segments, such as the N. Puerto Ayora Fault, have oscillatory throw patterns (Fig. 7) indicating that the fault is composed of multiple segments that have linked during the growth of the fault (Watterson, 1986). The longest fracture segment identified in the south is 5 km. The total fault lengths are likely always a minimum estimate; because most of the major faults have non-zero throw where they meet the coastline (e.g., Fig. 7), they probably extend offshore where the ocean obscures them.

3.1.2.1. Dated Faults

Three faults from the Southern group were selected for cosmogenic exposure dating (Fig. 4A). Our goal is to constrain the minimum age of the structures as well as to determine slip rates along each fault. From north to south, the dated faults are the Puerto Ayora Fault, the

Tortuga Bay Trail Fault, and the Iglesia de Santa Cruz Fault (Fig. 4A). For the Puerto Ayora and the Tortuga Bay Trail Faults, total throw was measured at 500 m intervals along strike using the DEM (Fig. 7). The Iglesia de Santa Cruz Fault has total throws less than the resolution of the DEM and is therefore omitted from our compilation (Table 1).

3.1.2.1.1. Puerto Ayora Fault

The Puerto Ayora fault trends on average 108° and extends a minimum of 5.8 km (Fig. 4A). The fault is on the south central flank of Santa Cruz Island and defines the northern boundary of the town of Puerto Ayora (Fig. 4A). The Puerto Ayora Fault is the northern fault of a graben valley, where the town of Puerto Ayora sits (Figs. 3, 4). The maximum throw along the fault is 25 m. Throw is distributed unevenly along strike with two local maxima, one about 2 km from the western fault tip and the other about 4.5 km from the same fault tip (Fig. 7).

3.1.2.1.2. Tortuga Bay Trail Fault

The Tortuga Bay Trail Fault trends 115° and extends a minimum of 3.2 km. The fault is located just south of Puerto Ayora (Fig. 4). The north-facing Tortuga Bay Trail Fault serves as the conjugate fault to the Puerto Ayora Fault that defines the graben in which the town is located. There is a paved walkway running orthogonal to the fault's strike that passes over the scarp near its southern extent. Furthermore, the boundary of the Galápagos National Park runs along strike with the fault at the base of the monocline that bounds it. There is a trail maintained by the park along this boundary as well. The combination of the Tortuga Bay trail and the boundary trail provides 1.5 km of along-strike exposure of the fault on the hanging wall side of the fissure, with more limited access on the footwall side. The maximum throw along the fault is 17 m, measured along the island's southern coastline, but continues to increase as it enters the ocean. Assuming that throw is distributed with the maximum throw at the mid-length of the fault, I project the measured length, at 2.3 km, to be less than half of the total. Thus, the Tortuga Bay trail fault is at least 4.6 km long.

3.1.2.1.3. Iglesia de Santa Cruz Fault

The Iglesia de Santa Cruz Fault trends 104° and is located within the graben formed by the Puerto Ayora Fault and the Tortuga Bay fault. The fault begins just west of Puerto Ayora and extends into the town where traces of the fault are visible in vacant lots and crossing through properties, including directly in front of a church, known locally as the "Iglesia de Santa Cruz". Because development of Puerto Ayora has obscured the fault's full extent, it has been mapped using an aerial photograph from 1985 (d'Ozouville et al., 2008b). Throw along the Iglesia de Santa Cruz Fault never exceeds 5 m. The maximum throw is 3.5 m (Profile 7 within Fig. 6; Table 1).

3.1.3. Monogenetic Vents

We have mapped the location of monogenetic vents shown as filled grey polygons and pit craters, hollow polygons, which are concentrated predominantly along the W-E trending spine of the island (Fig. 3). The surface area-weighted directional distribution of the mapped features is 95° (Fig. 5). Although there are visible deviations from circular footprints of volcanic vents, I do not document these orientations. In contrast, pit craters, which are products of subterranean magma evacuation, are elongate in the orientation of magma storage (e.g., Wyrick et al., 2004). In addition, pit craters tend to form chains parallel to their elongation direction (Wyrick et al., 2004). Therefore, I calculated the mean orientation of pit crater alignments and elongations, which is 86°.

3.2. Geochronology

3.2.1. ^{40}Ar/^{39}Ar Ages

Of the 15 samples collected for ^{40}Ar/^{39}Ar dating, 11 produced plateau ages (Table 2; Figs. 3, 4, 8). I report the uncertainties of all ages as 2σ. Samples SC12-012, 024, 070, 584B either yielded negative plateau ages or plateau ages discordant with isochron ages; I consider these results to be uninterpretable and do not discuss these analyses further. The plateau ages vary from 1620 ± 30 to 74 ± 38 ka. In general, the dates fall within those of Santa Cruz Island lavas determined by previous studies (Kurz and Geist, 1999; White et al., 1993) (Fig.

9), but the new ages, for the most, part have significantly smaller uncertainties. Notably, there is a gap in ages from 1160 ± 70 to 699 ± 36 ka (Fig. 9). The oldest four ages are all from the northeastern flank of Santa Cruz Island (Fig. 3, 4B). Furthermore, all samples with ages younger than 100 ka are located on the island's southern flank, consistent with previous observations (Cox and Dalrymple, 1966; Kurz and Geist, 1999; White et al., 1993).

3.2.1.1. Faults

Several dates provide insight into formation ages for the Southern Fault system (Figs. 4, 8). The Puerto Ayora Fault was dated twice. Sample SC12-011 is the uppermost basalt flow cut by the Puerto Ayora Fault and has a plateau age of 74 ± 38 ka. Thus, SC12-011 represents a maximum formation age for the fault at this location. Sample SC12-572B is a second flow collected on the footwall side of the Puerto Ayora fault and is the uppermost lava flow in the stratigraphy at the sampling site. The SC12-572B lava flowed into >10 cm wide joints in the underlying lava flow (SC12-572A; Fig. 17). Since filling in the joints of 572A, the Puerto Ayora fault has offset both flows SC12-572A and B. Although undated, the underlying lava flow (SC12-572A) has identical major and trace element compositions to SC12-572B (Wilson, 2013), and likely belongs to the same eruptive event. I make this assumption given the wide array of compositions erupted on Santa Cruz Island, even over short time scales (Bow, 1979; White et al., 1993; Wilson, 2013). If I assume that the dilation of joints in lava flow SC12-572A is a product of extension along the Puerto Ayora Fault, this $^{40}Ar/^{39}Ar$ age may indicate that 10 cm of dilation occurred along the fault contemporaneous with the eruption of SC12-572B at 416 ± 36 ka. However, since there is no indication that the lava flowed down a monocline formed by the fault, or off of the modern fault scarp, most, if not all displacement must have occurred after that date.

The uppermost lava flow on the northeast corner of Santa Cruz Island (SC12-060; Fig. 4), which was deformed by a fault belonging to the Northern Fault Group, yields an age of 1160 ± 70 ka (Fig. 8). Given that the fault deforms the lava, the age of this lava represents the maximum age for the sampled fault's formation.

Sample SC12-015 yields an age of 257 ± 112 ka, which provides a maximum age for the Tortuga Bay Trail Fault (Figs. 4, 8). I collected the sample on the uppermost lava flow on the hanging wall side of the Tortuga Bay Trail Fault.

3.2.1.2. Pit Craters and Monogenetic Cones

We collected sample SC12-027 from the wall of a pit crater locally known as 'Camote' (Fig. 3), which produced a plateau age of 208 ± 14 ka (Fig. 8). The lava flow is located approximately 88 m from the top of the pit crater. This result indicates that the upper ~100 m of volcanic material near the island's summit was erupted within the past 200 ka.

Near the island's summit, there is an open pit scoria quarry where two samples were collected. The first, SC12-040, is from the uppermost pile of scoria within the quarry and has an age of 271 ± 14 ka. The ~1 m thick lava flow that caps the cinder cone yielded a plateau age of 125 ± 31 ka.

3.2.2. Helium Isotopic Ratios

The $^3He/^4He_i$ ratios measured in the surface exposure samples exhibit only slight variations, from 6.3 to 8.8 R_a (Table 3). These values are interpreted to represent the magmatic $^3He/^4He_i$ ratio, with MORB-like signature, undisturbed by cosmic ray production of ^3He (Kurz, 1986a). The $^3He/^4He_i$ ratios reported here extend the range measured on Santa Cruz Island but overlap with those reported from elsewhere on the island (8.58 and 9.5 R/R_a; Kurz and Geist, 1999).

3.2.3. Surface Exposure Ages

We collected a total of twelve samples for surface exposure dating along three major faults exposed around the town of Puerto Ayora. The exposure ages (Table 4) are divided into four groups according to the primary fault from which they were sampled (Fig. 11).

3.2.3.1. North Puerto Ayora Fault

For all five of the samples collected on the North Puerto Ayora Fault (Fig. 4A), it was impossible to match the sampling face to its respective surface on the adjacent fissure wall. Samples along the Puerto Ayora Fault were taken from both the hanging wall and footwall sides of the fissure. The ages vary from 27 ± 17 ka to 115 ± 18 ka, with a weighted mean

age of 38 ± 8 ka (Fig. 11). There is no clear age progression from east to west along the fault, with all dates falling within error of one another, with one exception. Sample SC12-589, collected from the footwall side of the North Puerto Ayora Fault where the fault meets the ocean, yielded an age of 115 ± 18 ka; this is more than twice as old as the mean age calculated for the other samples. Notably, SC12-589 is also the only sample from more than ~1 km away from any other sampled locations along the same fault. The variation in ages across the fault suggests that faulting may have begun on the eastern flank of the island and migrated westward with time.

3.2.3.2. Tortuga Bay Trail Fault

Three samples were collected along the Tortuga Bay Trail Fault (Fig. 4A). Two of the three samples were from sites adjacent to each other within the same fissure, where one massively jointed lava flow detached along a cooling joint. The ages of these two samples should, therefore, be identical to one another and represent the faulting event. The sample from the hanging wall side of the fissure, SC12-016, is 34 ± 5 ka, and the adjacent sample from the footwall side of the fissure SC12-614 is 33 ± 10 ka (Fig. 11). Perhaps fortuitously, once corrected for shielding, the two samples' ages are statistically indistinguishable from each other. I collected the third sample from the Tortuga Bay Trail Fault (SC12-610) less than one kilometer southeast of the other two, which yielded an age of 48 ± 8 ka (Fig. 11). Therefore, I calculate a weighted mean age using all three samples from the Tortuga Bay Trail Fault of 38 ± 18 ka, which is coeval with the formation of the North Puerto Ayora Fault.

3.2.3.3. Iglesia de Santa Cruz Fault

Two samples (584A and 584B) were from the Iglesia de Santa Cruz Fault; I analyzed each of these twice (Fig. 4A; Table 3). Both samples were from the same fissure, one from the hanging wall and one from the footwall, and from the same lava flow. Furthermore, the joint pattern in the basalt could be matched up on both sides of the fissure. Therefore, the two samples should have an identical exposure history, representing the age of the fault. When corrected for shielding, the two are indistinguishable from each other at 81 ± 13 ka and 78 ± 12 ka, respectively. In contrast, by omitting the shielding correction, the calculated ages are significantly different from one another (Fig. 11). The disparity in the calculated ages when I

ignore the shielding correction helps to validate our shielding correction methods. The samples have a weighted mean age of 79 ± 12 ka with shielding. The average age of the Iglesia de Santa Cruz Fault is about twice that of the much larger faults to its north and south.

3.2.3.4. Well Fault

Two samples were collected from the Well Fault, which produced both the youngest and oldest exposure ages of any of the Santa Cruz Island faults in this study, at 16 ± 4 ka and 247 ± 38 ka (Fig. 11). The samples were located less than 10 m from each other (Fig. 4A). Given the disparity between the ages, a weighted mean age was not calculated for the Well Fault. The younger of the samples, SC12- 611A at 16 ± 4 ka, was collected from the footwall side of the Well Fault's fissure. I interpret the young age SC12-611A as the product of recent erosion of the fissure wall, or that the shielding is underestimated relative to that of other sample. In either case, I interpret that its age does not reflect the original faulting event. Instead, the older age of SC12-611B at 247 ± 38 ka is considered the formation date of the Well Fault in this location, as well as the maximum age recorded for the initiation of faulting on the island's southern flank.

3.3. Gravity Survey

3.3.1. Free Air and Bouguer Anomalies

There are 70.6 mGal of variation in the measurements of the free air anomaly across Santa Cruz Island. The FAA values are positively correlated with the island's elevation (Fig. 12). Values of FAA along the N-S transect increase gradually from the north coast southward, reaching a maximum of 1820 mGal just north of the island's summit. The values then decrease progressively to a low of 1749 mGal at the island's southern shoreline (Fig. 12). The E-W transect exhibits similar variations in FAA, with strong positive correlations between elevation and FAA values from W-E. The largest deviations from linearity of the FAA with elevation occur at ~400 m and near sea level (Fig. 12).

We chose 2400 kg/m^3 as the best fit for the island's density to calculate the final Bouguer Anomaly (BA). Of five BA anomalies calculated using island densities between 2000 and 2800 kg/m^3, 2400 kg/m^3 produced a BA anomaly that was least correlative to elevation (Fig. 14). In contrast to the FAA, the BA results exhibit a weak negative correlation with elevation, with the highest values on the southern flank of the island. Along the N-S transect, there are approximately 15 mGal of variation between the highest and lowest calculated values. Broadly, the N-S BA transect consists of a low BA near the crest of the island, midway along the N-S transect near the summit. As a result, BA intensity also decreases with increasing proximity to the highest concentration of monogenetic cones at the island's summit (Fig. 2, Fig. 13). North of the central gravity anomaly low, the BA increases to its maximum of 8 mGal and then decreases again to the lowest recorded values (-10 mGal) along the northern shoreline. South of the low anomaly at the island's crest, the BA gradually increases toward the southern shoreline. The increase in BA to the south correlates with the increase in deformation (i.e., abundance of faults and fissures) that is observed in the south (Fig. 4A). By comparison, the northern flank, where BA values decrease rapidly with proximity to the shoreline, the BA values increase steadily toward the southern shoreline near Puerto Ayora.

Along the W-E transect, BA values vary less than on the N-S transect (~9 mGal; Fig. 13). However, there is a significant increase in the BA from -4 mGal in the east to approximately 1 mGal near the center of the island, with a sharp spike to 4 mGal ~ 5 km east of the summit of the survey. From the local high of 4 mGal, the BA anomaly returns to ~1 mGal and remains similar for all of the measurements along the eastern survey (Fig. 13). Both the N-S and E-W transects record a similar sharp increase in BA at about 350 m elevation on the northern and eastern flanks.

3.3.2. Density Anomalies

The primary objective of the gravity inversion is to explore what types of density anomalies (negative or positive) and what magnitudes (in kg/m^3) are necessary to reproduce the BAs observed in the data.

First, I varied the depth of prisms that had a vertical thickness of 500 m, to explore the variation in width and magnitude of the resulting density anomaly (Fig. 15 A, B, C). By

varying the depth of the 500 m thick density anomaly between 0 and 1 km beneath the volcano surface (Fig. 15), the maximum density necessary to reproduce the BA data ranges from ~150 kg/m^3 to ~90 kg/m^3. As expected, there is a negative correlation between the depth and magnitude of the density anomaly. As the prisms are moved to greater depths, the locus for the maximum density anomaly shifts from the northern flank toward the island's summit (Fig. 15 A, C). When the prisms are directly beneath the surface of the island (0 m depth), the high-density anomaly is centered ~3 km N of the island's summit. Moreover, at shallow depths (0 and 500 m), two gravity anomalies of the same magnitude are needed to produce both the high BA values near the summit of the volcano and the high on the southern flank. In contrast, at a depth of 1000 m, only one density anomaly is required to produce the measured BA pattern along the N-S transect. That is, there are fewer high-density anomalies on the south flank compared to when the inversion is run at zero depth. It is particularly important to note that a negative density anomaly is never needed to generate the negative BA values at the summit of the island, regardless of the values of the other parameters.

The predicted maximum density anomaly is a linear function of the prism thickness (Fig. 15 A, D, E, F). For example, when the prisms are 500 m thick, the maximum density anomaly near the island's summit is approximately 150 kg/m^3. At twice the thickness (1000 m), the maximum density anomaly at the same location is reduced to ~80 kg/m^3. In all cases for a given depth to the top of the prisms, however, varying the dense object's thickness does not alter the shape of the resulting gravity anomaly.

In general, the depth and thickness of the prisms used in our model drastically change the magnitude of the calculated density anomaly (Fig. 15). The widths of the resulting density anomalies are nearly identical between all inversions, regardless of the input parameters. One density anomaly >15 km wide centered at the island's summit characterizes the W-E transect (Fig. 15 D). In contrast, there are two density anomalies within the N-S transect. Of the two anomalies, the first is ~5 km wide and centered 3-5 km north of the island's summit. The second density anomaly is >10 km wide and is located beneath the island's southern flank.

Chapter 4: Discussion

Eastern volcanoes in the Galápagos Archipelago are morphologically distinct from their western counterparts (Fig. 2). The absence of calderas, coupled with the presence of linear vent systems and normal faults are the primary observations that set the eastern Galápagos volcanoes apart from the volcanoes in the west (Figs. 1, 2). In addition the eastern volcanoes are active far beyond the predicted shutdown timing of the western Galápagos volcanoes based on proximity to the hotspot (e.g., Wilson, 2013; Geist et al., 2014b). Our goal in this study is to constrain the volcanic and structural histories of Santa Cruz Island determine the reason for the extended volcanic activity across the archipelago and to define the evolutionary processes responsible for the morphological differences between eastern and western Galápagos volcanoes.

4.1. Magmatic History

Our new ages record a history of volcanism on Santa Cruz spanning ~1600 ka (Figs. 8, 9), with the oldest sample dated to 1620 ± 30 ka. These ages are all younger than the oldest probable emergence age for the island of 2300 ka (Geist et al., 2014a). However, three of the samples from this study are older than any previous dates for Santa Cruz Island, extending active volcanism an additional 300 ka beyond what was previously recorded (White et al., 1993). All lavas collected for this study were erupted when Santa Cruz was located at or beyond the eastern extent of the western shield province (i.e., location of Alcedo; Figs. 1,2).

All Santa Cruz Island lavas erupted between 1620 ± 30 and 1160 ± 70 ka are classified on the basis of major, trace, and isotopic ratio signatures as Platform Series lavas (Wilson, 2013). Given this, the $^{40}Ar/^{39}Ar$ ages from this study constrain the eruption of the Platform Series to between 1620 ± 30 and 1160 ± 70 ka. The oldest sample, SC12-020 (1620 ± 30 ka; Fig. 8), was erupted when Santa Cruz Island was 86 km west of its present location (Fig. 20; Argus et al., 2011). This distance is equivalent to the current site of Alcedo volcano (Fig. 2). By the time Santa Cruz produced the last lavas of the Platform Series (1160 ± 70 ka; Fig. 8), the island was between present day Alcedo and Santiago Island (Fig. 20; Argus et al., 2011). According to the model proposed by Geist et al. (2014b) for the evolution of the western volcanoes, Santa Cruz should have been in the Dying Cooling Phase of volcanism

when it was erupting the Platform Series lavas. Our new ages, however, indicate that Platform Series volcanism on Santa Cruz continued an additional 0.46 Ma. Original age data (e.g., Bow, 1979; White et al., 1993) inspired Wilson (2013) to propose that Santa Cruz experienced a more gradual shut down process than is the case for current western shields, renaming it the Slow Dying Phase. Our new ages more precisely constrain the duration of the Slow Dying Phase on Santa Cruz Island in comparison to previous estimates.

When combined with previous work on Santa Cruz, our new data document a hiatus in volcanism between 1160 ± 70 and 699 ± 90 ka (Figs. 8, 9). The gap may represent a period of volcanic repose for Santa Cruz; alternatively, it may be the result of incomplete sampling of the island. Given the prevalence of lavas available both before and after the age gap (Fig. 9), however, it is unlikely that by chance, a period of ~500 ka went completely unsampled. Furthermore, the age gap is apparent in previous geochronological data sets, which also lack reliable (<50% 2σ uncertainty) age data between ~500 and 1000 ka (Bailey, 1976; Bow, 1979; Cox and Dalrymple, 1966). I propose that the gap simply went unnoticed in previous studies owing to both large uncertainties of K-Ar ages <1000 ka, as well as a lack of sampling resolution of the >1500 ka material on the island (5 samples; Kurz and Geist, 1999; White et al., 1993). Most importantly, the respite in volcanism between 1160 ± 70 ka and 699 ± 90 ka serves as a temporal boundary between the chemically distinct Platform and Shield Series lavas (White et al., 1993; Bow, 1979; Wilson, 2013). Interestingly, the oldest sample within the Shield Series (sample SC12-012) does not fall along the chemical trend defined by either the Platform or Shield Series suites (e.g., Fig. 18), further justifying the separation of the Platform and Shield Series by this hiatus.

The most recent phase of volcanism on Santa Cruz Island occurred from 699 ± 90 to 24 ± 11 ka (Figs. 8, 9). All lavas from this phase are all classified on the basis of their chemical compositions as Shield Series lavas (White et al., 1993; Wilson, 2013). Shield Series volcanism began when Santa Cruz was 36 km west of its present location (Fig. 20). This volcanic period continued effectively to the island's present location (Fig. 20). Our data indicate that volcanism during this phase was focused along the E-W trending summit vent system by 271 ± 17 ka and continued there until at least 125 ± 31 ka (Fig. 3).

There is a broad spatial migration of volcanism indicated by the Shield Series lavas. Lava flows erupted between 780 ka and 220 ka, dated using a combination of paleomagnetic

(Bow, 1979), [3]He systematics (Kurz et al., 1999; Kurz, *pers. comm.,* 2012*),* K-Ar (White et al., 1993), and this study, have been found on both the northern and southern flanks of the island. In contrast, samples younger than 220 ka are concentrated on or south of the summit vent system (Fig. 3; Kurz, *pers. comm.,* 2012; White et al., 1993). These observations indicate that by 220 ka, volcanism on Santa Cruz was migrating south of the summit vent system, concentrating lava flows onto the southern flank.

To summarize, all lavas from this study were erupted when Santa Cruz Island was east of the current location of the western Galápagos shield volcanoes (Figs. 2, 20). The most recent Santa Cruz lavas were deposited in two phases separated by a period of volcanic repose between 1160 ± 70 and 699 ± 90 ka (Fig. 9). Platform Series lavas were produced between 1620 ± 30 and 1160 ± 70 ka (Fig. 20). Volcanism during the Platform Series was extended an additional 460 ka beyond the Dying Cooling Phase proposed for Galápagos volcanoes by Geist et al. (2014b). Shield Series volcanism occurred between 699 ± 90 and 24 ± 11 ka (minimum age from White et al., 1993). Shield Series lavas between the ages of 699 ± 90 and ~200 ka are found on both the northern and southern flanks of the island (Fig. 3). By 271 ± 14 ka, Shield Series volcanism was focused along the E-W trending summit vent system, where it remained active until ~100 ka. After 100 ka, Shield Series volcanism migrated south of the summit vent system.

4.2. Structural History

4.2.1. Northern Fault History

On the basis of crosscutting relationships, our [40]Ar/[39]Ar ages indicate that the Northern Fault system was active after 1160 ± 70 ka (Fig. 4). As a further constraint on the maximum age of fault formation, the Northern Faults deform normally polarized lavas (younger than 781 ka1; Bow, 1979). Therefore, I interpret that the maximum age of Northern Fault formation is 780 ka, consistent with the conclusion of Bow (1979).

We have little quantitative data to constrain the minimum age for Northern Faults. Given the lack of modal olivine in basalts of the intact fault scarps, exposure dating could not be conducted in the same manner as on the Southern Fault system. There are some lavas,

however, that flow around existing Northern Fault scarps (e.g., Bow 1979), which provide a lower age boundary to the faults. One of these lavas was dated (SC12-024, Fig. 3), but yielded an unreliable plateau age (Fig. 8). On the basis of weathering alone, the Northern Fault scarps appear older than the undeformed lava from sample SC12-024, which have a maximum formation age of 247 ± 38 ka (see next section). Given that the northern flank of Santa Cruz is more arid (~50 mm/yr of rainfall; Grant and Boag, 1980) than the southern flank (~400 mm/yr of rainfall; Grant and Boag, 1980), erosion rates are likely slower in the north than in the south. Nevertheless, the Southern Faults are in general better preserved than the Northern Faults, with the majority of the Northern Faults having been reduced to slopes of rubble (Fig. 16). From these observations, I conclude that the Northern Faults are at least older than the oldest Southern Faults (247 ± 38 ka; Figs. 4, 11).

4.2.2. Southern Fault History

Our ^{40}Ar/^{39}Ar ages provide a maximum limit for the deformation occurring along the Southern Faults of Santa Cruz Island. Deformation may have begun as early as 416 ± 36 ka, which is the oldest lava offset by a fault (Fig. 4). Furthermore, faulted lavas sampled near the Town of Puerto Ayora were dated at 257 ± 112 and 74 ± 38 ka. The lower age indicates that deformation was ongoing at least until 74 ± 38 ka.

Our helium exposure ages overlap the ^{40}Ar/^{39}Ar ages and corroborate the result that deformation by the Southern Faults occurred after 416 ± 36 ka and continued up to 38 ± 8 ka. A more detailed picture of fault formation chronology can be gleaned from the exposure age data. Our exposure ages indicate that the periphery of the sampling area contains the oldest fault scarps. Our oldest exposure age suggests faulting began at 247 ± 38 ka (Figs. 4, 11) on the western extent of the sampling area. The second oldest sample, SC12-589, is from the eastern edge of the sampling area, with an age of 115 ± 18 ka. All samples located between these two samples are younger, with average ages ranging between 79 ± 13 and 38 ± 5 ka (Fig. 11). Tight clustering of ages on the North Puerto Ayora Fault and the Tortuga Bay Trail Fault with average exposure ages of 38 ± 8 and 38 ± 18 ka indicate that the faults were formed synchronously, and are the last recorded deformation event, with a minimum formation age of 38 ± 8 ka. The use of ^{3}He thus allows us to set a minimum age of faulting which would not be possible using only ^{40}Ar/^{39}Ar in this scenario.

The tight clustering of ages near the town of Puerto Ayora helps to validate our methodology for sample collection and age calculation. I consider it to be highly unlikely that by chance I calculated synchronous ages for 7 samples (Fig. 11), had they not all been recording the same deformation event. On this basis, I take a step further to assume that the ages for the individual samples are the actual formation ages of the faults they were collected from. If I make this simplifying assumption for all of our exposure ages, having been validated for the faults near Puerto Ayora, I can bracket the formation of the Southern Faults between the maximum and minimum exposure ages on the southern flank as a whole. If I do this, I can bracket deformation between 247 ± 38 and 38 ± 8 ka. This age range is consistent with the ^{40}Ar/^{39}Ar results described above, but allows for a more precise duration to be interpreted.

4.3. Interpretation of Bouguer Anomaly and Gravity Inversion Results

The maximum BA calculated for Santa Cruz Island is ~14 mGal (Fig. 13). This value is half of what has been measured on Fernandina volcano in the western Galápagos (Ryland, 1975). For Fernandina, the density anomaly is interpreted as a volume of dense cumulates that underlies its subcaldera magma chamber (Geist et al., 2014b). In addition, Geist et al. (2014b) suggest that a simple cylinder can reproduce the measured density anomaly on Fernandina volcano. This assumes that the cumulate pile generating the density anomaly mimics the sill-like shape of western Galápagos magma reservoirs (Geist et al., 2006; Chadwick et al., 2011). Given that the BA for Santa Cruz Island is less than half of what is recorded on Fernandina, it is unlikely that a similarly sized cumulate body resides beneath Santa Cruz. Furthermore, the density anomaly beneath Santa Cruz is more complex than that underlying Fernandina, with multiple positive anomalies from N-S and an E-W elongation of the summit anomaly (Fig. 15). On the basis of these observations, I conclude that a large cumulate body, such as the sill-shaped magma chambers proposed for the western Galápagos shields, is not responsible for the BA beneath Santa Cruz.

An alternative source for the positive BA on Santa Cruz Island could be the solidified remains of the volcanic plumbing system for the island. Examples of this type of anomaly have been documented on other volcanic islands (e.g., Costa Rica, Thorpe et al., 1981; Hawaii, Kinoshita, 1965). In Costa Rica, Thorpe et al. (1981) record a BA anomaly of 10 mGal near the summit of the volcano, which closely aligns with our results. On this basis I

propose that the BA detected at Santa Cruz is more likely produced by shallow intrusions than a cumulate body.

If I assume that solidified volcanic conduits are responsible for the BA beneath Santa Cruz Island, then the inversion results for zero depth density anomalies should provide the most accurate assessment of the locations and sizes of the density anomalies beneath Santa Cruz (Fig. 15A). Along the E-W gravity transect (Fig. 15A), there is a single density anomaly >15 km wide. Along the N-S transect, there are two separate density anomalies. The first is located just north of the island's summit and is 5 km wide. The second density anomaly is beneath Puerto Ayora, and continues to rise beyond the southern extent of the gravity survey, making it >10 km in width.

The elongate shape of our anomalies resemble observations from Hawaii and the Azores (Ablay and Kearey, 2000; Kinoshita, 1965). On these islands, density anomalies are interpreted as high concentrations of intrusions and other magmatic bodies (Ablay and Kearey, 2000; Kinoshita, 1965; Malengreau, 1999; Rousset et al., 1989). In Hawaii, the orientations of the density anomalies are interpreted as representing the strike of subsurface rift system (e.g., Fiske and Jackson, 1974 and references therein). Linear vent patterns on each volcano's surface are mirrored in the subsurface by a positive BA that is parallel to vent alignments. Similarly, the elongation of the summit density anomaly (Fig. 15A) parallels the orientation of the summit vent system (Fig. 3). On the basis of these correlations, I conclude that the positive BAs on Santa Cruz are the result of the solidified remains of the magmatic plumbing system. Our gravity data indicate that most recently preserved plumbing system on Santa Cruz Island was complex, and not sourced from a single shallow magma reservoir, which is consistent with the conclusions of Wilson (2013).

4.4. Evolution of Santa Cruz Island

On the basis of our results, the volcanic and structural histories of Santa Cruz Island are more complicated than proposed by previous researchers (Bow, 1979; Swanson et al., 1974). The most recent volcanism on the island occurred in two temporally distinct phases, according to our $^{40}Ar/^{39}Ar$ results (Fig. 9). The first phase of volcanism is the Platform Series, lasting from 1620 ± 30 ka to 1160 ± 70 ka, and the second is the Shield Series, from 699 ± 90 to 24 ± 11 ka. Furthermore, faulting on Santa Cruz Island can also be categorized into

two separate phases. The Northern Faults formed between 780 and 247 ± 38 ka and the Southern Faults formed between 247 ± 38 and 38 ± 8 ka. The new structural, geophysical and geochronological data can be used to construct an updated evolutionary history of Santa Cruz Island, with a focus on the origins of the extended volcanism and the formation mechanisms of the Northern and Southern Faults.

4.4.1. Origins of Extended Volcanism

Geist et al. (2014b) propose that western Galápagos shield volcanoes enter a Dying Cooling Phase about 1000 ka after emergence (e.g., Alcedo Volcano). Basaltic volcanism on Santa Cruz Island, however, extends more than 1500 ka beyond this stage (Fig. 20). Wilson (2013) previously attributed prolonged volcanism on Santa Cruz to the volcano's position on thinner lithosphere during its more recent history (Wilson, 2013). Lithospheric thickness beneath the eastern Galápagos is ~10 km thinner than under the western volcanoes (Feigner and Richards, 1994; Villagomez et al., 2007). Wilson (2013) proposed adding a final category to the Geist et al. (2014b) classification of western volcanoes; the Slow Dying Phase includes all eastern volcanoes with extended volcanic activity (Wilson, 2013). From our age data I constrain the Slow Dying Phase to extend volcanism 460 ka beyond the Dying Cooling Phase of Alcedo (Fig. 20).

The Shield Series volcanism began after a repose period of ~400 ka (Fig. 11). The Slow Dying Phase hypothesis of Wilson (2013) does not provide an explanation for this hiatus. Compared to Platform Series lavas, Shield Series lavas are less voluminous (Bow, 1979), more alkalic, and have more depleted radiogenic isotopic signatures (Fig. 18; Wilson, 2013). These characteristics are reminiscent of Hawaiian rejuvenated volcanism (e.g., Walker, 1987; Clague and Dalrymple, 1988; Lipman et al., 1989). In Hawaii, a gap of 250 to 2500 ka separates primary shield-building volcanism from subsequent rejuvenated volcanism (e.g., Clague and Dalrymple, 1987; Garcia et al., 1987; Ozawa et al., 2005; Garcia et al., 2010). Other volcanic island chains exhibit similar hiatuses in eruptive activity, including Samoa (e.g., Konter and Jackson, 2012), Mauritius (Moore et al., 2011), and the Canary Islands (e.g., Paris et al., 2005). In Hawaii, rejuvenated volcanism is significantly less voluminous than the primary shield-building phase (Walker, 1990). Rejuvenated lavas are moderately to strongly alkalic (e.g., Lipman et al., 1989) and are isotopically more depleted than shield series lavas (e.g., Clague and Dalrymple, 1988). I propose that Shield Series volcanism on

Santa Cruz Island is a rejuvenated phase of volcanism that follows initial shut-down of the main shield activity.

Our identification of a rejuvenated phase of volcanism is the first of its kind in the central Galápagos Archipelago. Although recent evidence for late-stage volcanism in the southern Galápagos has been identified on Floreana Island (Harpp et al., 2014), its origins have been attributed to chemical heterogeneity in the plume, not mechanisms typically associated with rejuvenescent volcanism at other island chains (e.g., Ribe and Christensen, 1999; Bianco et al., 2005). The characteristics of Santa Cruz Shield Series lavas are more consistent with Hawaiian rejuvenescence than what Harpp et al. (2014) observe on Floreana Island. Several competing proposals exist to explain rejuvenated volcanism in Hawaii and other hotspot provinces. Ribe and Christensen (1999) attribute rejuvenescence to a secondary melting zone related to the interaction of the spreading mantle plume and the overlying lithosphere. Alternatively, Bianco et al. (2005) suggest that flexural arch decompression is responsible for rejuvenated volcanism. Although beyond the scope of this paper, our data circumstantially favor the flexural arch hypothesis to generate Santa Cruz Shield Series lavas. There is structural evidence for regional uplift immediately prior to Shield Series volcanism (Section 4.3.2.), which may have initiated decompression melting. Furthermore, melt depth estimates calculated using Sm/Yb ratios, and plotted against age (Fig. 19; Gibson and Geist, 2010) indicate that depths to the top of the melt column are widely variable during the Shield Series, but include the shallowest calculated depths from any samples collected on Santa Cruz (Wilson, 2013).

4.4.2. Origins of Structures

4.4.2.1. Northern Faults

Northern Fault throws increase toward the shoreline (Fig. 3). Assuming a fault's throw is normal about the initiation point of the feature (e.g., Watterson, 1986) the Northern Faults must have begun propagating at or beyond the island's shoreline. Moreover, the Northern Fault orientations are parallel to structures on nearby islands, such as Baltra, Seymour, and Santa Fe (Bow, 1979). Therefore, the stress field responsible for the formation of the Northern Faults was probably regional, and not locally generated by the volcanic edifice

(e.g., flank instability due to gravitational loading; e.g., Dietrich, 1988). The uniform orientation of the faults and the widespread distribution among multiple islands is more consistent with their formation in response to a regional, homogeneous stress field (e.g., Hjartardóttir et al., 2012).

The Northern Faults exhibit a morphology and geometry that differs from faults elsewhere on the island. In contrast to the Southern Faults, the Northern Faults are more eroded and have a more uniform orientation (Fig. 5). These results indicate that the Northern Faults formed during a separate deformation episode than the Southern Faults, within a stress field of a different orientation.

Previously, Swanson et al. (1974) invoked upward flexure of the Galápagos Platform in response to the underlying mantle plume as a source for regional stress, forming the Faults on Santa Cruz and similarly oriented structures on San Cristobal and Santa Fe Islands. Furthermore, Bow (1979) documented a history of subsidence and reemergence of Santa Cruz Island, in which he attributed the reemergence of the island to regional uplift associated with the formation of the Northern Faults. According to his integrated paleomagnetic and stratigraphic data, Bow (1979) concluded that uplift occurred before 500 ka. Because the minimum and maximum ages of Bow (1979) are narrower than the 780 to 247 ± 38 ka interval I propose on the basis of the new geochronological data, I use the more precise 500 ka of Bow (1979) as the lower age boundary for the formation of the Northern Faults.

We propose that the Northern Faults formed in response to regional extensional stresses between 780 ka and 500 ka (ages from Bow, 1979). The regional uplift of the Galápagos Platform during this time is responsible for the formation of the Northern Faults, consistent with proposals of Swanson et al. (1974) and Bow (1979). Most notably, the hiatus in volcanism between 1160 ± 70 ka and 699 ± 90 ka coincides with the formation of the Northern Faults. If the younger boundary for Northern Fault formation could be better constrained by $^{40}Ar/^{39}Ar$ or exposure dating, the significance of this relationship could be more thoroughly addressed. Regardless, our data are consistent with the hypothesis that faulting on Santa Cruz may be the physical expression of flexural uplift, which in turn may have initiated the rejuvenated Shield Series volcanism (Sec. 4.5.1).

4.4.2.2. Southern Faults

The Southern Faults contrast with the Northern Faults in their morphology, distribution on the island (Fig. 3), and orientations (Fig. 5). The Southern Faults are broadly E-W trending in the center of the southern deformation zone, closest to the island's summit (Fig. 3). The Southern Faults form a concave-outward distribution, and faults trend NE on the southwestern flank but NW on the southeastern flank (Fig. 3). This concentric distribution may indicate that the Southern Faults formed in a local stress field induced by the volcanic edifice. This mechanism better explains the similarity of the faults to the shape of the island. Gravitational stresses alone would not be strong enough to cause such deformation on Santa Cruz, however, because its flanks are shallower than the angle of repose for volcanic islands (8-20°; Iverson, 1991; e.g., Iverson, 1992).

A different mechanism that commonly induces flank deformation on volcanic islands is magmatic intrusion (Moore et al., 1989). On the Big Island of Hawaii, for example, extension is accommodated by vertical fissures on the volcano's surface and is oriented nearly horizontal at the volcano's base, making them listric in shape (Dieterich 1988). The listric shape can cause faults to face both toward and away from the volcano's summit (Le Corvec and Walter, 2009). On Hawaii, normal faults propagate upward from depth forming monoclinal folds, which are eventually breached by vertical fissures (Peacock and Parfitt, 2002; Martel and Langley, 2006). Moreover, the faults are concentric about Kilauea volcano (Martel and Langley, 2006). The Southern Faults on Santa Cruz exhibit similar orientations (Figs. 3, 4, 5). Consequently, I interpret that a comparable mechanism may have been responsible for the Southern Faults.

The coincidence between the formation of the Southern Faults and the migration of magmatism from the summit vent system is compelling evidence that faulting was induced by magmatic activity. Our ^{40}Ar/^{39}Ar ages record that magmatism along the summit rift system of Santa Cruz was occurring by 271 ± 14 ka and continued until ~100 ka, when it migrated south of the island's summit (Sec. 4.2; Fig. 3). This timeframe is similar to the two oldest exposure ages of the Southern Fault System of 247 ± 38 and 115 ± 18 ka. I suggest that during this interval, flank spreading accommodated extension within the volcano generated by E-W intrusions supplying the southern vent system (Figs. 3, 5; e.g., Dieterich et al., 1988).

A shift in volcanism from the summit vent system toward the island's southern flank occurred ~100 ka, according the new $^{40}Ar/^{39}Ar$ ages (Sec 4.2; Fig. 3). The positive BA beneath the island's southern flank (Fig. 13), which I interpret as the remnants of the magmatic plumbing system, is consistent with this interpretation. It is possible that the southward motion of the southern flank reoriented the stress field within the volcanic edifice, which in turn redirected magmatism from the summit vent system toward the island's southern flank. Consistently, there is a nearly synchronous cessation of magmatism at 24 ± 11 ka (White et al., 1993) and fault formation at 38 ± 8 ka. The dynamic response between flank instability and reorientation of eruptive features is commonly observed at other volcanic structures, including Hawaii (e.g., Le Corvec and Walter, 2009) and the Canary Islands (e.g., Walter et al., 2004), and is consistent with observations at Santa Cruz.

4.5. Morphological Variation of Galápagos Island Volcanoes

The extended volcanic activity of Santa Cruz Island does not explain the striking morphological differences between eastern and western Galápagos volcanoes. Instead, I propose that the morphological distinctions are the result of the island's proximity to or distance from the plume.

Using our age data, the maximum volume flux for rejuvenated volcanism on Santa Cruz Island can be compared to the shield-building phases of Fernandina. Santa Cruz Island has a subaerial volume of`~297 km^3. I assume that the carapace of the rejuvenated phase of volcanism on Santa Cruz Island (Shield Series) is 400 m thick at the summit (maximum estimate; Bow, 1979), thinning to 0 m at the flank (since pre-rejuvenated lavas are observed on the shoreline; Fig. 3). From this I assume that the remaining volume is of pre-rejuvenated lava, giving a subaerial volume of the rejuvenated phase of 137 km^3. Since Shield Series volcanism began at 699 ± 90 ka (Fig. 9) the maximum time averaged volume flux for the rejuvenated volcanism is 0.20 km^3/ka, using the subareal volume I cite above.

Fernandina has a time averaged eruption rate since emergence of 4.4 km^3/ka (Kurz et al., 2014). The minimum volume flux for Fernandina is more than 20 times greater than what I calculate as a maximum volume flux for the rejuvenated phase of volcanism on Santa Cruz Island. Given the low volume flux, it is unlikely that the rejuvenated phase of volcanism on Santa Cruz Island was supplied by the long-lived, shallow magma chamber necessary to

generate the calderas characteristic of the western volcanoes (e.g., Acocella, 2007; Naumann and Geist, 2000). Consistently, our data indicate that the rejuvenated volcanism on Santa Cruz is manifested as monogenetic cones along a linear vent system, not from a centralized source (Figs. 3, 5; e.g., Walker, 2000). Furthermore, lavas erupted during the Shield Series exhibit a wide range of compositions consistent with generation at a variety of depths (e.g., Fig. 18; Wilson, 2013) (Fig. 19), which also supports that lavas are not being erupted from a central magma chamber.

Once magma supply rates decrease beyond a certain threshold, continued low flux magmatism shifts the volcano from a western to an eastern morphological character. It is plausible that the long duration of extended and rejuvenated volcanism (>1.5 My, ≥ 80 m thick near the summit), could erase any evidence of a previously existent caldera. While long term subsidence (> 500 m for Santa Cruz; Geist et al., 2014a), could explain the variations in height between western and eastern volcanoes.

Chapter 5: Conclusions

Our results indicate that there were two phases of extended volcanism on Santa Cruz
Island, separated by a hiatus in activity. The first phase of volcanism, which produced the
Platform Series lavas (Bow, 1979), was erupted between 1620 ± 30 and 1160 ± 70 ka. This
phase extends 460 ka after the predicted Dying Cooling Phase of the western Galápagos
volcanoes (Geist et. al., 2014b), currently exhibited by Alcedo Volcano on Isabela Island.
Consistent with the conclusions of Wilson (2013), the extension of volcanism on Santa Cruz
(the Slow Dying Phase of Wilson, 2013) is caused by the migration of Santa Cruz Island
onto thinner lithosphere, resulting in melt generation at shallower depths and greater
distances from the Galápagos hotspot.

A period of quiescence between 1160 ± 70 and 699 ± 90 ka follows the Platform Series. Our
age data are consistent with the hypothesis that during this time, there was regional uplift of
the Galápagos Platform between 780 and 500 ka. I propose that the Northern Faults formed
in response to this regional uplift event. Although the cause of the regional uplift remains
undetermined, the timing of uplift is consistent with it being related to rejuvenated volcanism
beginning 699 ± 90 ka.

Shield Series volcanism, first defined by Bow (1979), is the most recent activity recorded on
Santa Cruz Island. Shield Series volcanism occurred between 699 ± 90 and 24 ± 11 ka
(minimum age from White et al., 1993). Our $^{40}Ar/^{39}Ar$ ages indicate that Shield Series
volcanism was focused along the prominent summit vent system by 271 ± 14 ka, where it
remained active until ~100 ka. After 100 ka, Shield Series volcanism migrated south of the
summit vent system. Two positive E-W trending BA highs have been identified beneath
Santa Cruz, one below the island's summit and the second on the southern flank. I propose
that these anomaly highs are caused by the solidified remains of the magmatic plumbing
system beneath the summit and the southern flank of the island after activity migrated
southward ~100 ka. Initiation of Shield Series volcanism may be a rejuvenescent phase
similar to those documented in Hawaii, the Canary Islands, and on other ocean islands (e.g.,
(Paris et al., 2005; Garcia et al., 2010; Konter and Jackson, 2012). The classification of
rejuvenated volcanism sub-divides Wilson's (2013) Slow Dying Phase into two temporally
distinct stages. The first is the Slow Dying Phase identified by Wilson (2013) and the second
is rejuvenated volcanism. Identification of a rejuvenated phase of volcanism on Santa Cruz

helps to reconcile the extended duration of Galápagos volcanism in comparison to what is observed in Hawaii.

Exposure dating of the normal faults on the southern flank of Santa Cruz yielded formation ages coeval with the latest extent of Shield Series volcanism, between 247 ± 38 and 115 ± 18 ka. The faults have a mean orientation parallel to the size-weighted mean orientation of the summit vents and are symmetric about the summit of the volcano. I conclude that the faults formed to accommodate spreading within the edifice after the E-W trending summit rift was established. The timing of fault formation and the migration of volcanism from the summit vent system toward the southern flank are coincident. Therefore, spreading may have reoriented the stress field within the volcanic edifice, favoring a shift in magmatism toward the southern flank. Cessation of fault formation at 38 ± 8 ka is also nearly coincident with the eruption of the youngest dated lava on the island of 24 ± 11 ka, corroborating the link between the two processes (e.g., Fiske and Jackson, 1972; Le Corvec and Walter, 2009; Walter et al., 2004).

The extended volcanism phases on Santa Cruz Island are significantly lower flux (~0.20 km^3/ka) than that of the western volcanoes (>4.7 km^3/ka). Given such low volume fluxes during the Slow Dying and rejuvenated phases, Santa Cruz cannot support a shallow magma chamber and thus do not produce caldera forming eruptions. Instead, eruptions are focused along vent patterns oriented parallel to E-W trending regional or local (gravitational) maximum compressive stresses. Once established, magmatism along these primitive summit rift zones may induce flank instability, producing faults to match. These faults further distinguish the eastern volcanoes from their western counterparts morphologically. Combined, the subsidence of Santa Cruz over time and the persistence of extended volcanism over >1 My would be enough to obliterate any evidence of early phases of volcanism, including any caldera forming phases. Other volcanoes in the eastern Galapagos experiencing similar durations of extended volcanism (Santiago, San Cristobal) presumably undergo similar evolutions.

Our analysis indicates that much remains to be discovered from detailed analysis of individual volcanoes in the Galápagos Archipelago (e.g., Wilson, 2013; Harpp et. al., 2014). In particular, many questions remain in terms of our understanding of the long-term evolution of Galápagos volcanoes (Geist et al., 2014b). The multidisciplinary integration of

^{40}Ar/^{39}Ar and cosmogenically produced ^{3}He dating techniques with structural and gravity observations permits reconstruction of volcanic histories in considerable detail. This approach could prove to be invaluable in future studies of other not-so-typical ocean islands in the Galápagos or elsewhere in the world.

Works Cited

Ablay, G. J., & Kearey, P. (2000). Gravity constraints on the structure and volcanic evolution of Tenerife, Canary Islands. *Journal of Geophysical Research: Solid Earth (1978–2012)*, *105*(B3), 5783–5796.

Acocella, V., Korme, T., & Salvini, F. (2003). Formation of normal faults along the axial zone of the Ethiopian Rift. *Journal of Structural Geology*, *25*(4), 503–513.

Argus, D. F., Gordon, R. G., & DeMets, C. (2011). Geologically current motion of 56 plates relative to the no-net-rotation reference frame. *Geochemistry, Geophysics, Geosystems*, *12*(11). doi:10.1029/2011GC003751

Bailey, K. (1976). Potassium-argon ages from the Galapagos Islands. *Science*, *192*(4238), 465–467.

Balco, G., Stone, J. O., Lifton, N. a., & Dunai, T. J. (2008). A complete and easily accessible means of calculating surface exposure ages or erosion rates from 10Be and 26Al measurements. *Quaternary Geochronology*, *3*(3), 174–195. doi:10.1016/j.quageo.2007.12.001

Bow, C. S. (1979). *Geology and petrogenesis of lavas from Floreana and Santa Cruz Islands, Galápagos Archipelago, Ecuador*. University of Oregon, Eugene, OR, USA.

Carracedo, J. C. (1999). Growth, structure, instability and collapse of Canarian volcanoes and comparisons with Hawaiian volcanoes. *Journal of Volcanology and Geothermal Research*, *94*(1-4), 1–19. doi:10.1016/S0377-0273(99)00095-5

Chadwick Jr, W. W., & Howard, K. A. (1991). The pattern of circumferential and radial eruptive fissures on the volcanoes of Fernandina and Isabela islands, Galapagos. *Bulletin of Volcanology*, *53*(4), 259–275.

Chadwick, W. W., & Dieterich, J. H. (1995). Mechanical modeling of circumferential and radial dike intrusion on Galapagos volcanoes. *Journal of Volcanology and Geothermal Research*, *66*(1-4), 37–52. doi:10.1016/0377-0273(94)00060-T

Cox, A., & Dalrymple, G. B. (1966). Palaeomagnetism and potassium-argon ages of some volcanic rocks from the Galapagos Islands. *Nature*, *209*(5025), 776–777.

d'Ozouville, N., Auken, E., Sorensen, K., Violette, S., de Marsily, G., Deffontaines, B., & Merlen, G. (2008a). Extensive perched aquifer and structural implications revealed by 3D resistivity mapping in a Galapagos volcano. *Earth and Planetary Science Letters*, *269*(3-4), 518–522. doi:10.1016/j.epsl.2008.03.011

d'Ozouville, N., Deffontaines, B., Benveniste, J., Wegmüller, U., Violette, S., & de Marsily, G. (2008b). DEM generation using ASAR (ENVISAT) for addressing the lack of freshwater ecosystems management, Santa Cruz Island, Galapagos. *Remote Sensing of Environment*, *112*(11), 4131–4147. doi:10.1016/j.rse.2008.02.017

Dawers, N. H., & Anders, M. H. (1995). Displacement-length scaling and fault linkage. *Journal of Structural Geology*, *17*(5), 607–614.

Dieterich, J. H. (1988). Growth and persistence of Hawaiian volcanic rift zones. *Journal of Geophysical Research*, *93*(7), 4258–4270.

Dunne, J., Elmore, D., & Muzikar, P. (1999). Scaling factors for the rates of production of cosmogenic nuclides for geometric shielding and attenuation at depth on sloped surfaces. *Geomorphology*, *27*(1-2), 3–11. doi:10.1016/S0169-555X(98)00086-5

Fiske, R. S., & Jackson, E. D. (1972). Orientation and growth of Hawaiian volcanic rifts : the effect of regional structure and gravitational stresses. *Proceedings of the Royal Society of London. Series A. Math. and Phys. Sciences*, *329*(1578), 299–326.

Geist, D. J., Snell, H., Snell, H., Goddard, C., & Kurz, M. D. (2014a). A Paleogeographic Model of the Galápagos Islands and Biogeographical and Evolutionary Implications, *The Galápagos: A Natural Laboratory for the Earth Sciences, Geophysical Monograph 204* (First Edit., pp. 145–166). John Wiley & Sons, Inc.

Geist, D. J., Bergantz, G., & Chadwick, W. W. (2014b). Galápagos Magma Chambers. *The Galápagos: A Natural Laboratory for the Earth Sciences, Geophysical Monograph 204* (First Edit., pp. 55–70). John Wiley & Sons, Inc.

Goehring, B. M., Kurz, M. D., Balco, G., Schaefer, J. M., Licciardi, J., & Lifton, N. (2010). A reevaluation of in situ cosmogenic 3He production rates. *Quaternary Geochronology*, *5*(4), 410–418. doi:10.1016/j.quageo.2010.03.001

Graham, D. W., Christie, D. M., Harpp, K. S., & Lupton, J. E. (1993). Mantle plume helium in submarine basalts from the galapagos platform. *Science (New York, N.Y.)*, *262*(5142), 2023–6. doi:10.1126/science.262.5142.2023

Grant, P. R., & Boag, P. T. (1980). Rainfall on the Galapagos and the demography of Darwin's finches. *The Auk*, 227–244.

Harpp, K. S., Geist, D. J., Koleszar, A. M., Christensen, B., Lyons, J., Sabga, M., & Rollins, N. (2014). The Geology and Geochemistry of Isla Floreana , Galápagos : A Different Type of Late-Stage Ocean Island Volcanism. *The Galápagos: A Natural Laboratory for the Earth Sciences, Geophysical Monograph 204* (First Edit., pp. 71–118). John Wiley & Sons, Inc.

Harpp, K. S., & White, W. M. (2001). Tracing a mantle plume: Isotopic and trace element variations of Galapagos seamounts, *2*(2000).

Hjartardóttir, Á. R., Einarsson, P., Bramham, E., & Wright, T. J. (2012). The Krafla fissure swarm, Iceland, and its formation by rifting events. *Bulletin of Volcanology*, *74*(9), 2139–2153. doi:10.1007/s00445-012-0659-0

Kinoshita, W. T. (1965). A Gravity Survey of the Island of Hawaii '. *Pacific Science*, *19*, 339–340.

Kurz, M. D. (1986a). < i> In situ</i> production of terrestrial cosmogenic helium and some applications to geochronology. *Letters to Geochemica et Cosmochemica Acta*, *50*, 2855–2862.

Kurz, M. D. (1986b). Cosmogenic helium in a terrestrial igneous rock. *Nature*, *320*(3), 435–439.

Kurz, M. D., Kenna, T. C., Lassiter, J. C., & DePaolo, D. J. (1996). Helium isotopic evolution of Mauna Kea Volcano: First results from the 1-km drill core. *Journal of Geophysical Research: Solid Earth (1978–2012)*, *101*(B5), 11781–11791.

Kurz, M. D., Rowland, S. K., Curtice, J., Saal, A. E., & Naumann, T. (2014). Eruption rates for Fernandina volcano: a new chronology at the Galápagos hotspot center. *The Galapagos: A Natural Laboratory for the Earth Sciences*, *204*, 41.

Kurz, M., & Geist, D. (1999). Dynamics of the Galapagos hotspot from helium isotope geochemistry, *63*(23), 4139–4156.

Lal, D. (1991). Cosmic ray labeling of erosion surfaces:< i> in situ</i> nuclide production rates and erosion models. *Earth and Planetary Science Letters*, *104*(2), 424–439.

Le Corvec, N., & Walter, T. R. (2009). Volcano spreading and fault interaction influenced by rift zone intrusions: Insights from analogue experiments analyzed with digital image correlation technique. *Journal of Volcanology and Geothermal Research*, *183*(3-4), 170–182. doi:10.1016/j.jvolgeores.2009.02.006

Lipman, P. W., & Calvert, a. T. (2011). Early growth of Kohala volcano and formation of long Hawaiian rift zones. *Geology*, *39*(7), 659–662. doi:10.1130/G31929.1

Lipman, P. W., Lockwood, J. P., Okamura, R. T., Swanson, D. A. t, & Yamashita, K. M. (1985). Ground deformation associated with the 1975 magnitude-7.2 earthquake and resulting changes in activity of Kilauea volcano, Hawaii. *US Geol. Surv. Prof. Pap*, *501-D*, D95–98.

Mackey, B. H., Castonguay, S. R., Wallace, P. J., & Weldon, R. J. (2014). Synchronous late Pleistocene extensional faulting and basaltic volcanism at Four Craters Lava Field, central Oregon, USA. *Geosphere*, *10*(6), 1247–1254.

Malengreau, B. (1999). Structure of Reunion Island, Indian Ocean / inferred from the interpretation of gravity anomalies. *Journal of Volcanology and Geothermal Research*, *88*, 131–146.

Martel, S. J., & Langley, J. S. (2006). Propagation of normal faults to the surface in basalt, Koae fault system, Hawaii. *Journal of Structural Geology*, *28*(12), 2123–2143. doi:10.1016/j.jsg.2005.12.004

McBirney, A. R., & Williams, H. (1969). Geology and petrology of the Galapagos Islands. *Geological Society of America Memoirs*, *118*, 1–197.

Mittelstaedt, E., Soule, S., Harpp, K., & Fornari, D. (2014). Variations in crustal thickness, plate rigidity, and volcanic processes throughout the Northern Galápagos Volcanic Province. *The Galápagos: A Natural Laboratory for the Earth Sciences* (First Edit., pp. 263–284). John Wiley & Sons, Inc.

Moore, J. G., Clague, D. A., Holcomb, R. T., Lipman, P. W., Normark, W. R., & Torresan, M. E. (1989). Prodigious submarine landslides on the Hawaiian Ridge. *Journal of Geophysical Research: Solid Earth (1978–2012)*, *94*(B12), 17465–17484.

Morgan, W. J. (1972). Deep mantle convection plumes and plate motions. *AAPG Bulletin*, *56*(2), 203–213.

Nakamura, K. (1980). Why do long rift zones develop better in Hawaiian volcanoes: a possible role of thick oceanic sediments (in Japanese). *Journal of the Volcanological Society of Japan*, *25*, 255–267.

Naumann, T., & Geist, D. J. (2000). Volcano , Isabela Island , Galµpagos : implications for the development. *Bulletin of Volcanology*, *61*, 497–514.

Normark, W. R., & Torresan, M. E. (1989). Prodigious Submarine Landslides on the. *Journal of Geophysical Research*, *94*(89), 17,465–17,484.

Oehler, J.-F., Lénat, J.-F., & Labazuy, P. (2007). Growth and collapse of the Reunion Island volcanoes. *Bulletin of Volcanology*, *70*(6), 717–742. doi:10.1007/s00445-007-0163-0

Peacock, D. C. P., & Parfitt, E. A. (2002). Active relay ramps and normal fault propagation on Kilauea Volcano , Hawaii. *Journal of Structural Geology*, *24*, 729–742.

Pollard, D. D., Delaney, P. T., Duffield, W. A., Endo, E. T., & Okamura, A. T. (1983). Surface deformation in volcanic rift zones. *Tectonophysics*, *94*(1), 541–584.

Rousset, D., Lesquer, A., Bonneville, A., & Lénat, J. F. (1989). Complete gravity study of Piton de la Fournaise volcano, Réunion Island. *Journal of Volcanology and Geothermal Research*, *36*(1), 37–52.

Singer, B. S., & Pringle, M. S. (1996). Age and duration of the Matuyama-Brunhes geomagnetic polarity reversal from 40Ar/ 39Ar incremental heating analyses of lavas. *Earth and Planetary Science Letters*, *139*(96), 3–9.

Sinton, C. W., Christie, D. M., & Duncan, R. A. (1996). Geochronology of Galápagos Seamounts. *Journal of Geophysical Research*, *101*(B6), 13,689–13,700.

Stone, J. O. (2000). Air pressure and cosmogenic isotope production. *Journal of Geophysical Research: Solid Earth (1978–2012)*, *105*(B10), 23753–23759.

Swanson, F. J., Baitis, H. W., Lexa, J., & Dymond, J. (1974). Geology of Santiago, Rábida, and Pinzón Islands, Galápagos. *Geol. Soc. of America Bulletin*, *85*(11), 1803–1810.

Tentler, T., & Mazzoli, S. (2005). Architecture of normal faults in the rift zone of central north Iceland. *Journal of Structural Geology*, *27*(9), 1721–1739. doi:10.1016/j.jsg.2005.05.018

Thorpe, R. S., Locke, C. A., Brown, G. C., Francis, P. W., & Randal, M. (1981). Magma chamber below Poás volcano, Costa Rica. *J. of the Geol. Society*, *138*(3), 367–373.

Walker, G. P. L. (2000). Basaltic volcanoes and volcanic systems. *Encyclopedia of Volcanoes*, 283–289.

Watterson, J. (1986). Fault dimensions, displacements and growth. *Pure and Applied Geophysics*, *124*(1-2), 365–373.

White, W. M., & Hofmann, A. W. (1978). Geochemistry of the Galápagos Islands: implications for mantle dynamics and evolution. *Year Book Carnegie Inst. Washington*, *77*, 596–606.

White, W. M., McBirney, A. R., & Duncan, R. A. (1993). Petrology and geochemistry of the Galápagos Islands: Portrait of a pathological mantle plume. *Journal of Geophysical Research: Solid Earth (1978–2012)*, *98*(B11), 19533–19563.

Wilson, D. S., & Hey, R. N. (1995). History of rift propagation and magnetization intensity for the Cocos-Nazca sspreading Center. *Journal of Geophysical Research: Solid Earth (1978–2012)*, *100*(B6), 10041–10056.

Wilson, E. L. (2013). *The geochemical evolution of Santa Cruz Island, Galápagos Archipelago*. (K. S. Harpp, Ed.). University of Idaho.

Wyrick, D., Ferrill, D. A., Morris, A. P., Colton, S. L., & Sims, D. W. (2004). Distribution, morphology, and origins of Martian pit crater chains. *Journal of Geophysical Research: Planets (1991–2012)*, *109*(E6).

Fig. 1: Map of the Galápagos Archipelago. Santa Cruz Island and the location of Fig. 3 are in the center of the Archipelago. Absolute plate direction and motion for the Nazca Plate are calculated from Argus et al. (2011).
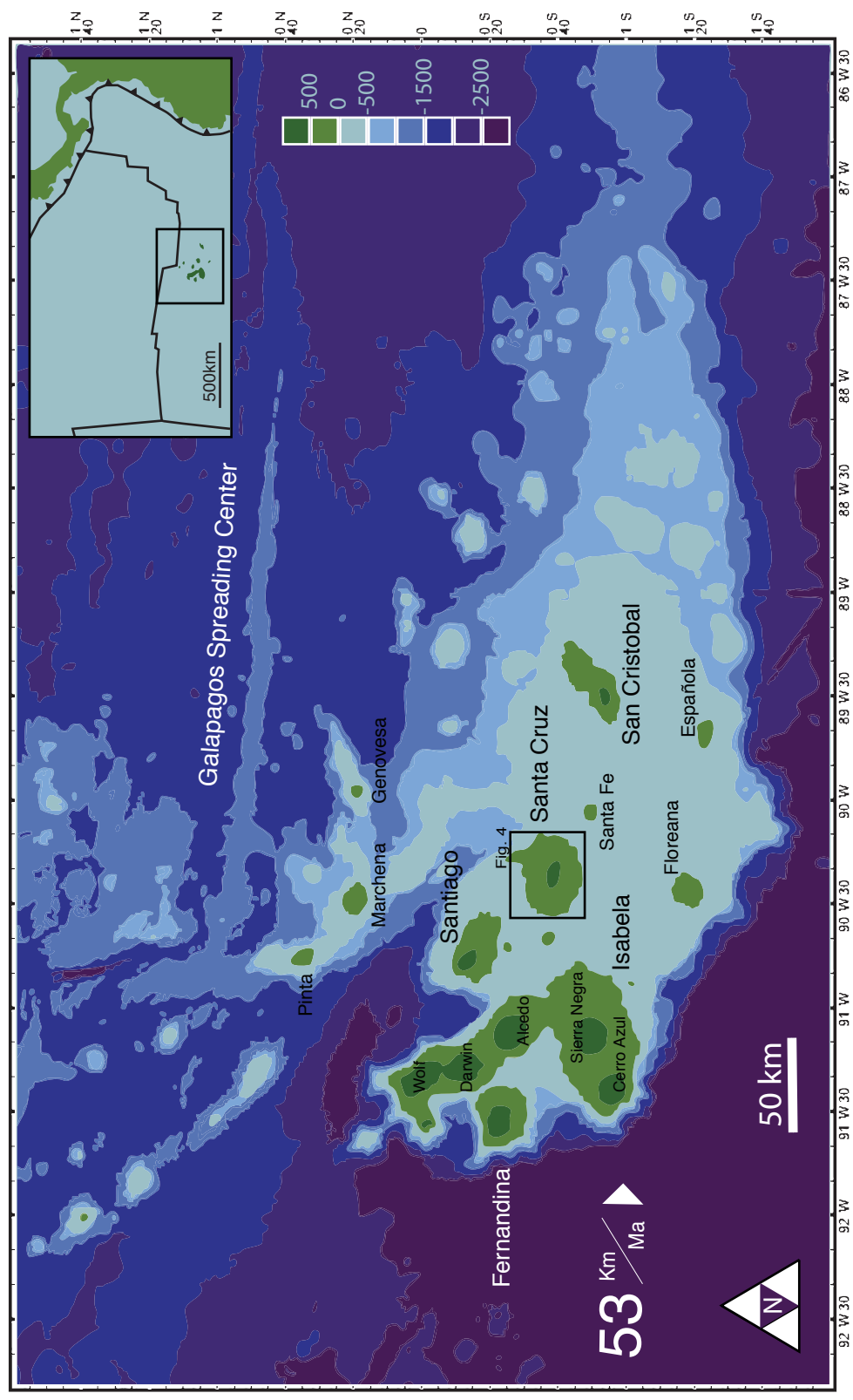
Fig. 2: Cross-section from W-E across the Galápagos Platform. Elevations of individual profiles for the islands along the cross-section are superimposed at the same horizontal and vertical scale. The inset shows the profiles of the islands along the transect superimposed upon one another, for comparison.
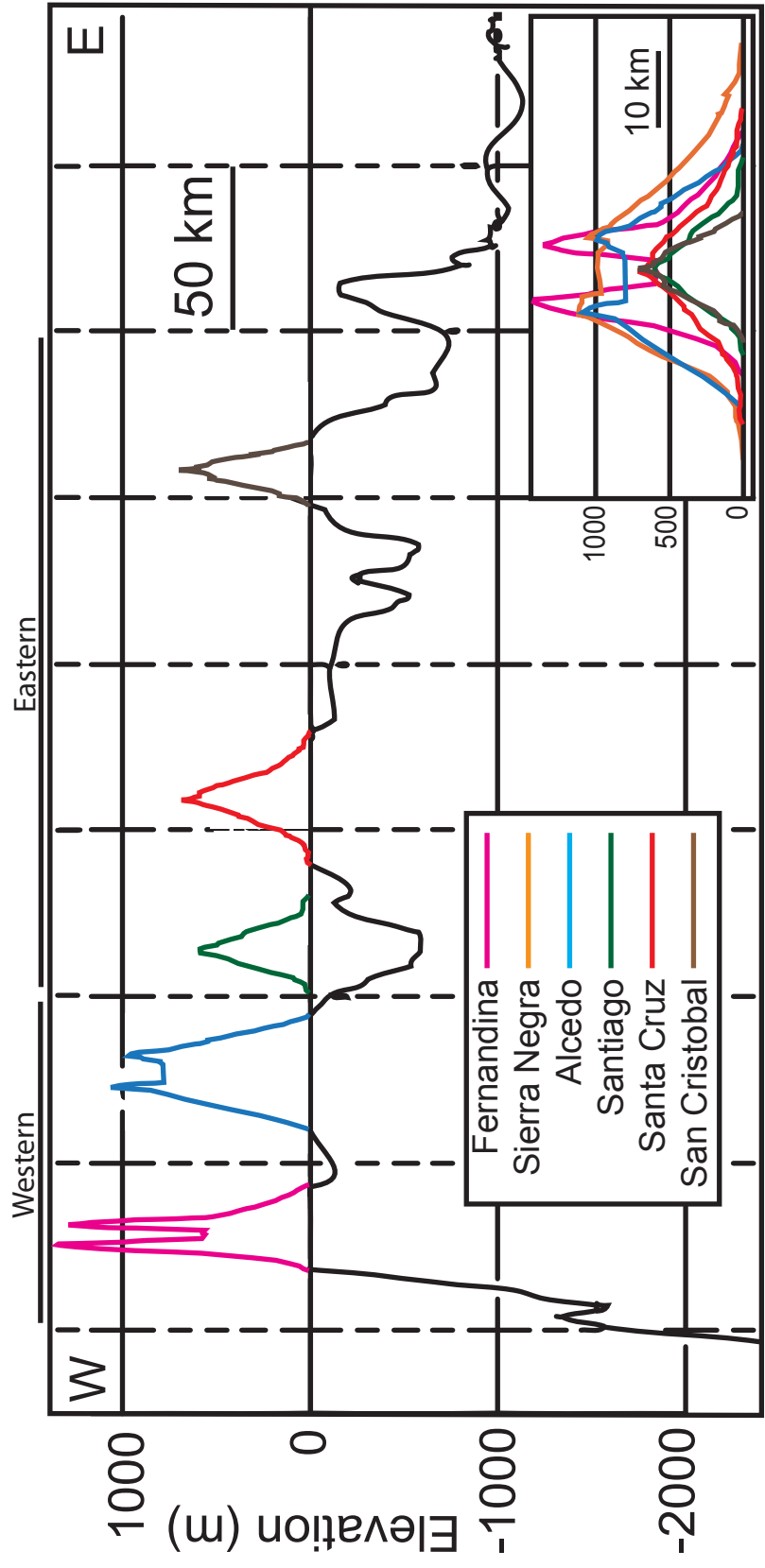
Fig. 3: Map of Baltra and Santa Cruz Islands illustrating prominent structural and volcanic features mapped using satellite data. Locations of gravity survey transects are indicated as colored lines. New ^{40}Ar/^{39}Ar age (ka) results from this study are in italics. Names for samples that are found in Fig. 4 insets are not labled on this map.
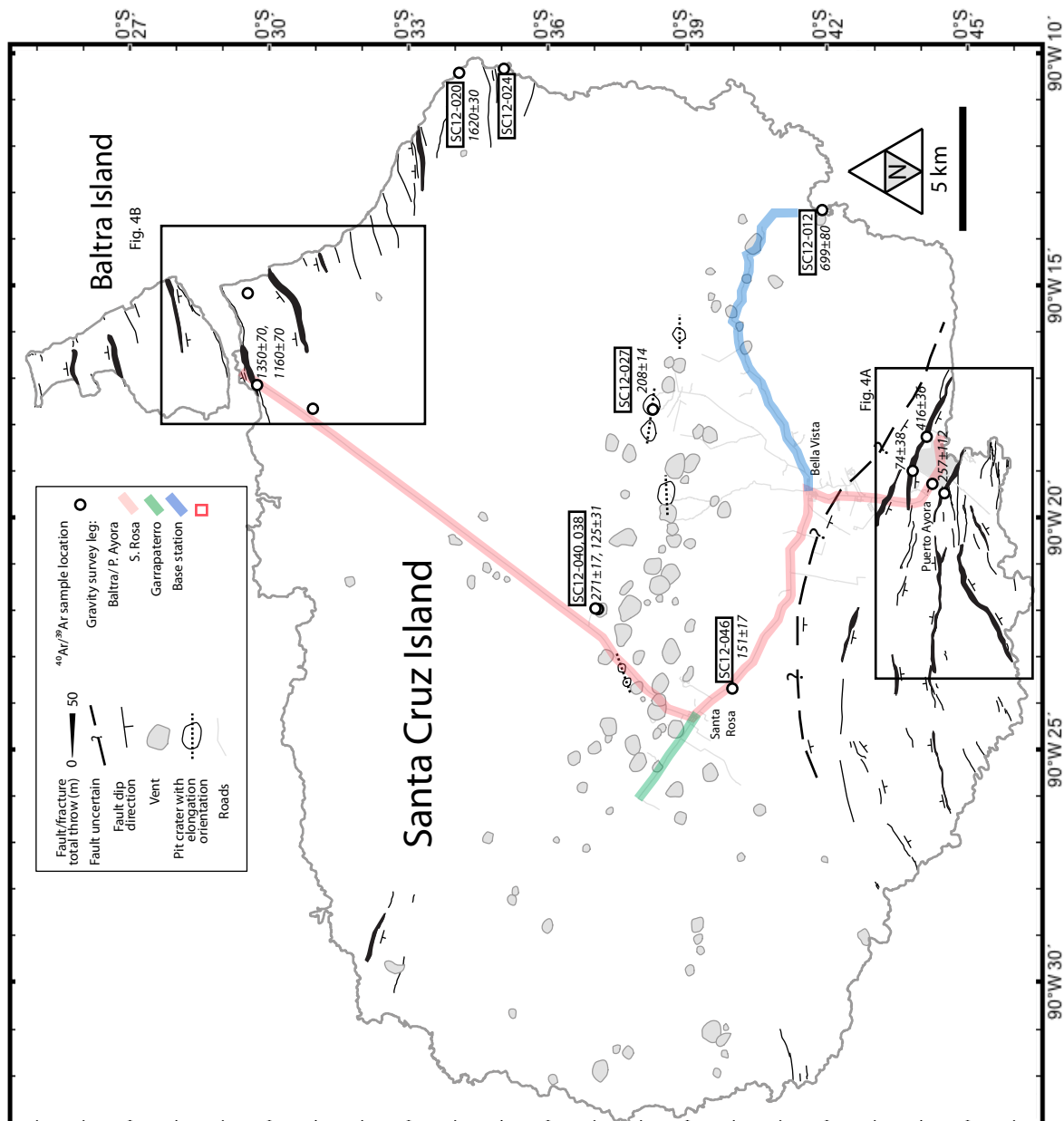
Fig. 4: Maps showing the locations of cosmogenic age samples and locations of GPS measurements from the southern (A) and northeastern (B) quadrants of Santa Cruz Island (Fig. 3). Primary faults are highlighted in yellow. Sample locations are marked in red. GPS traverses are displayed as dotted lines and are labeled with a circled number corresponding to their respective profiles in Fig. 6. New ^{40}Ar/^{39}Ar age (ka) results from this study are in italics. Other symbols correspond to those found in the Fig. 3 legend.
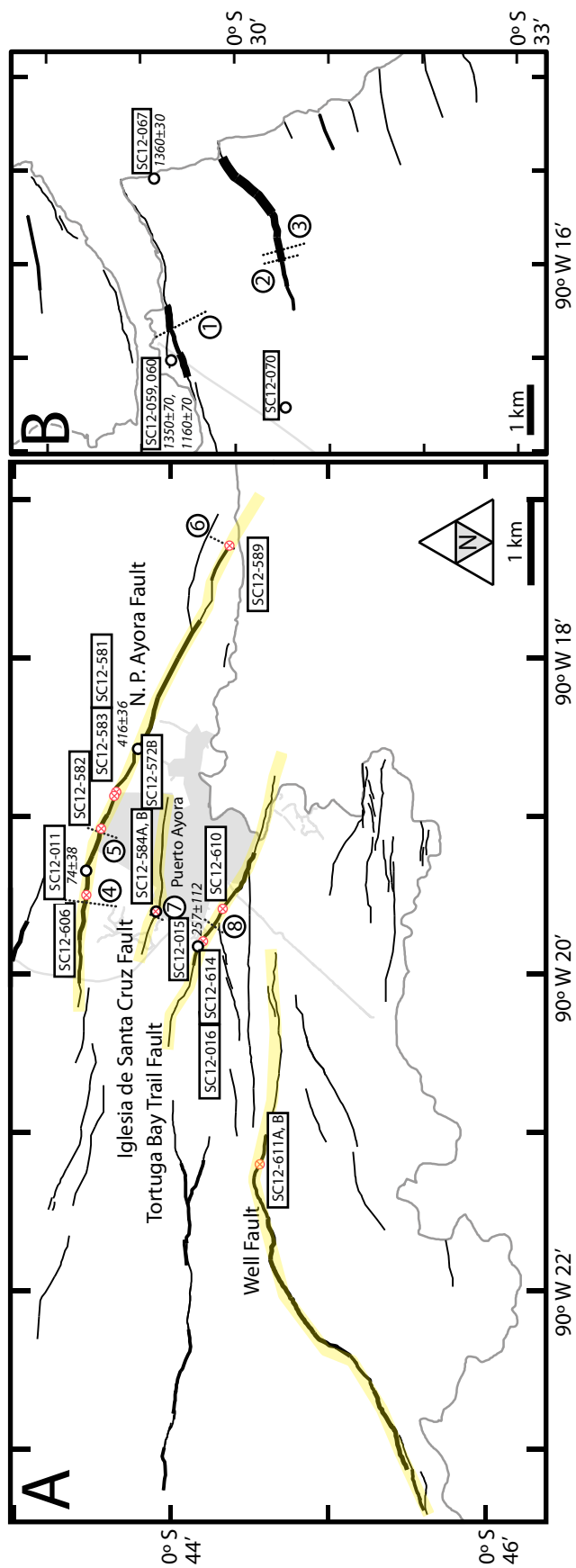
Fig. 5: Rose diagram summarizing the orientation of prominent structural features on Santa Cruz Island and relevant regional features. The orientations of the Southern Faults are in yellow and the Northern Faults are in blue. The orientation of the GSC is shown as a solid grey line. The solid green line is the surface area weighted directional distribution of vents (VD). The dashed black arrow indicates direction of plate motion for the Nazca Plate (NZ).
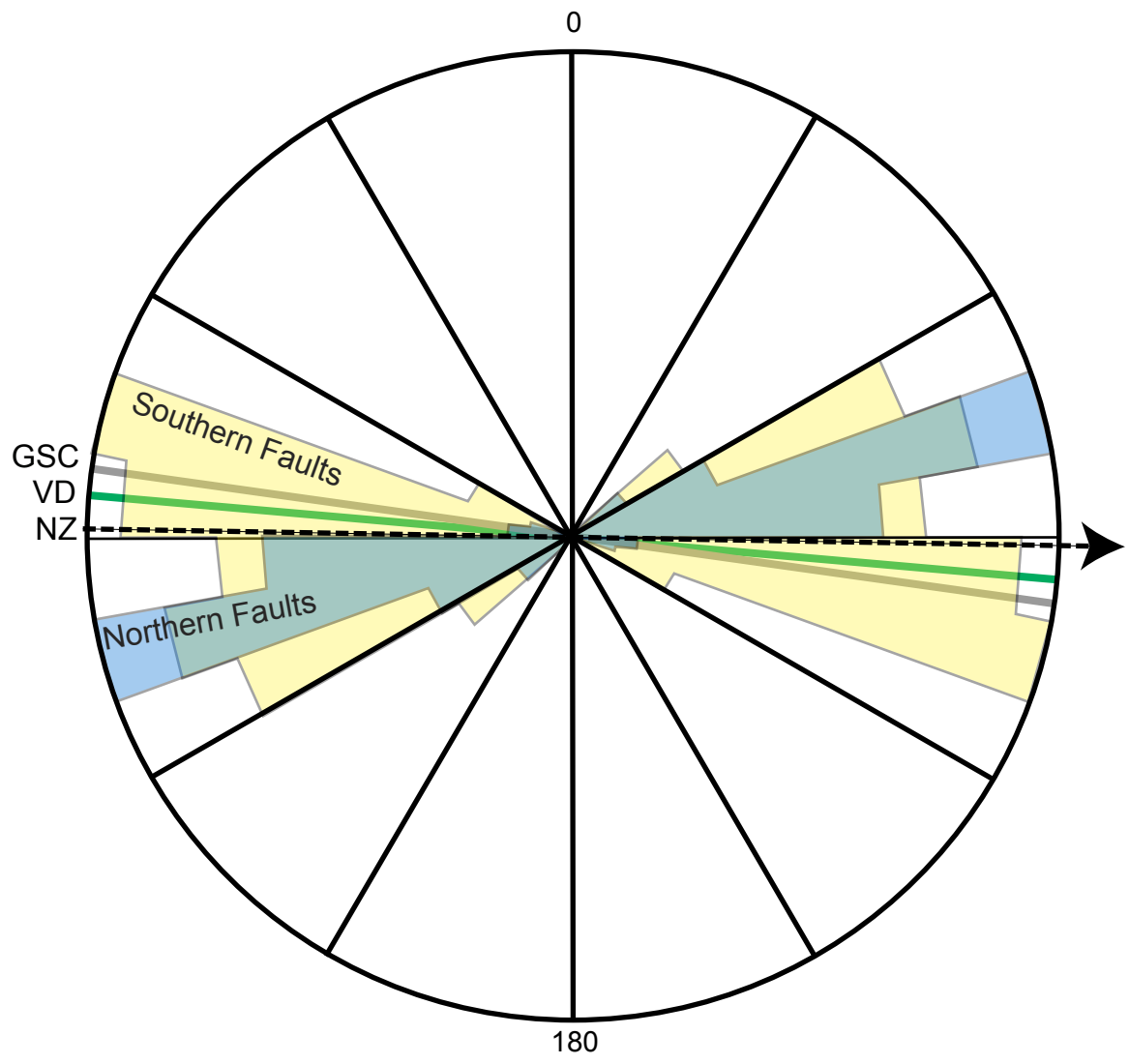
Fig. 6: Profiles of fault throw orthogonal to fault strike. Distance along the y-axis is from north to south, with zero representing the location of the fault scarp. Throw along the y-axis is plotted in meters relative to the center of the fault scarp. Locations of corresponding throw profiles are shown in Fig. 4. Elevations measured in the field using GPS are represented as black circles and elevations interpolated from the DEM are dashed lines.

Fig. 6: (continued)

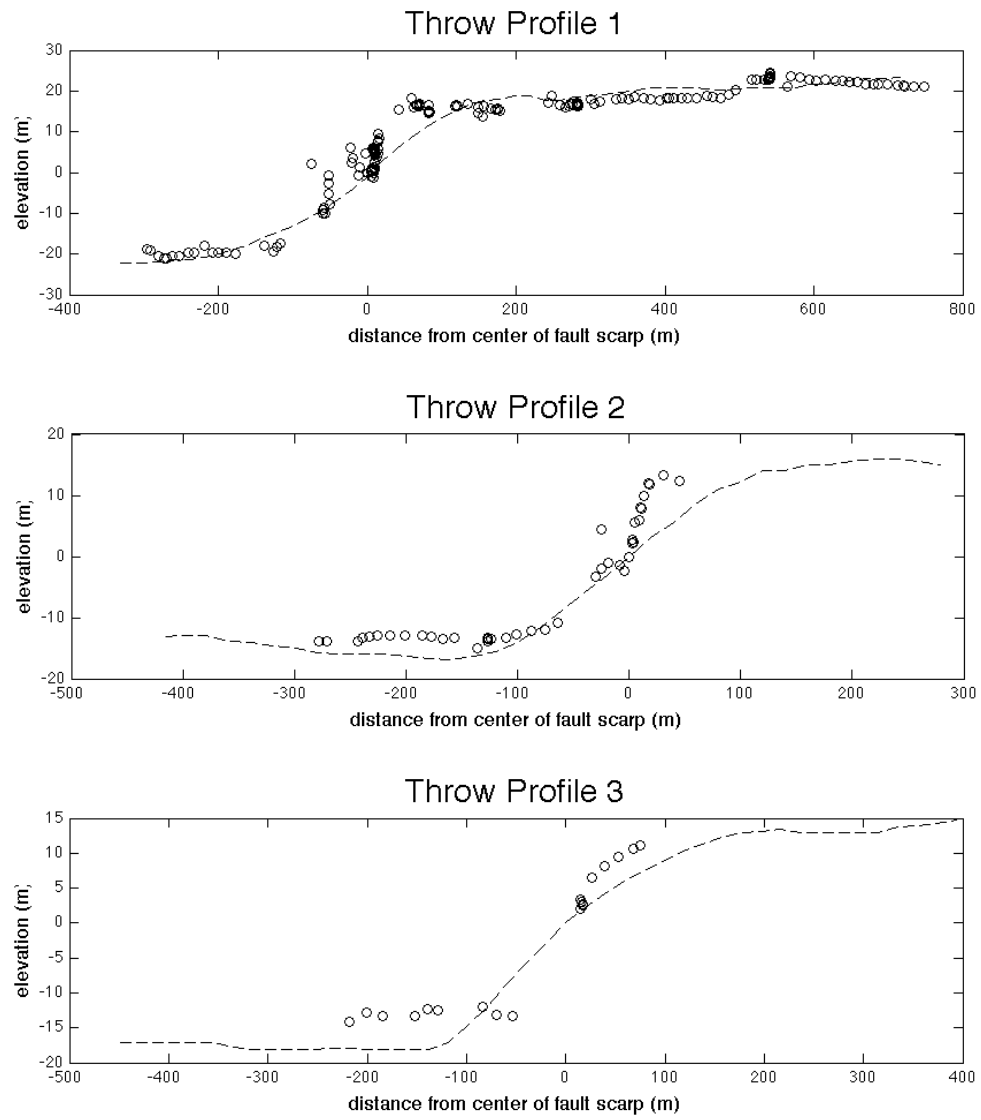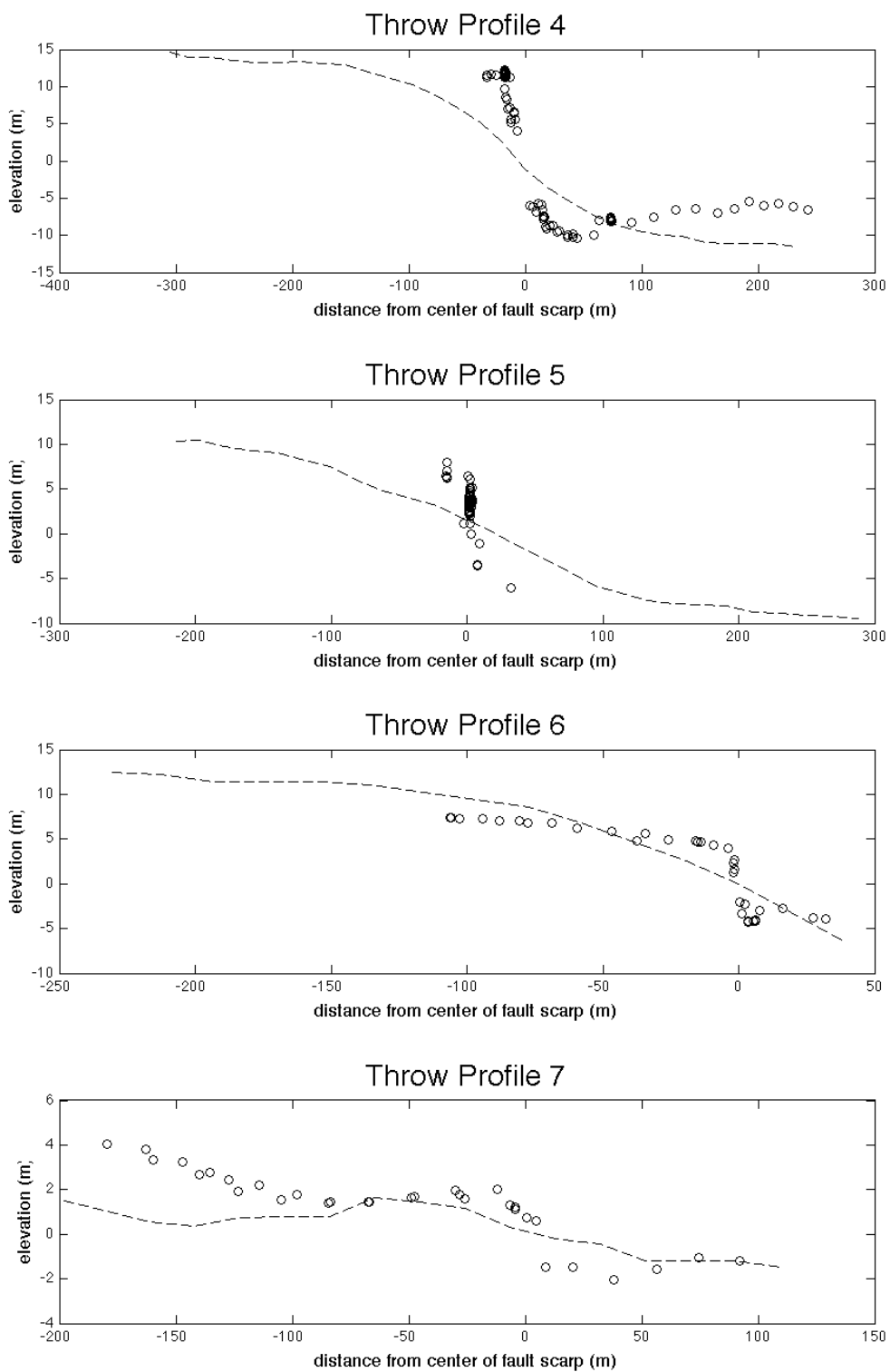

Throw Profile 4

Throw Profile 5

Throw Profile 6

Throw Profile 7

Fig. 6: (continued)
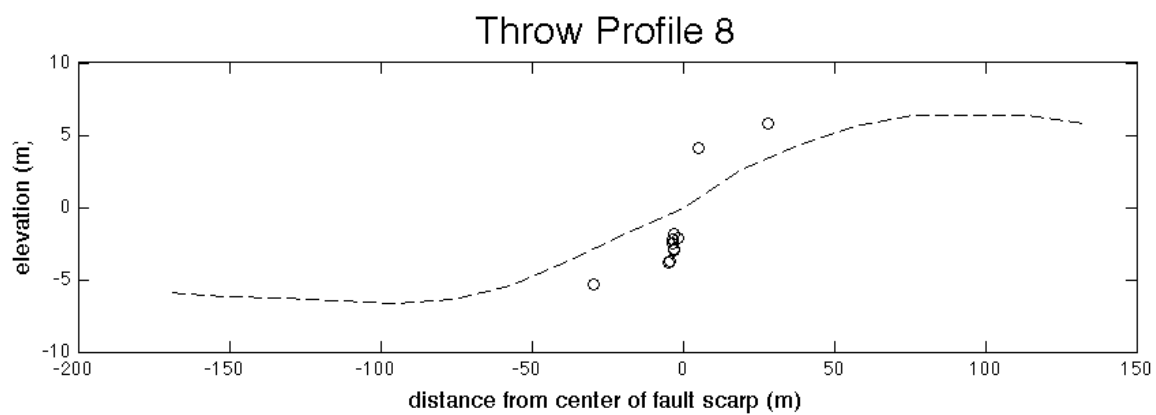

Throw Profile 8

Fig. 7: Profiles of fault throw measured along strike for the Puerto Ayora Fault (top) and the Tortuga Bay Trail Fault (bottom).
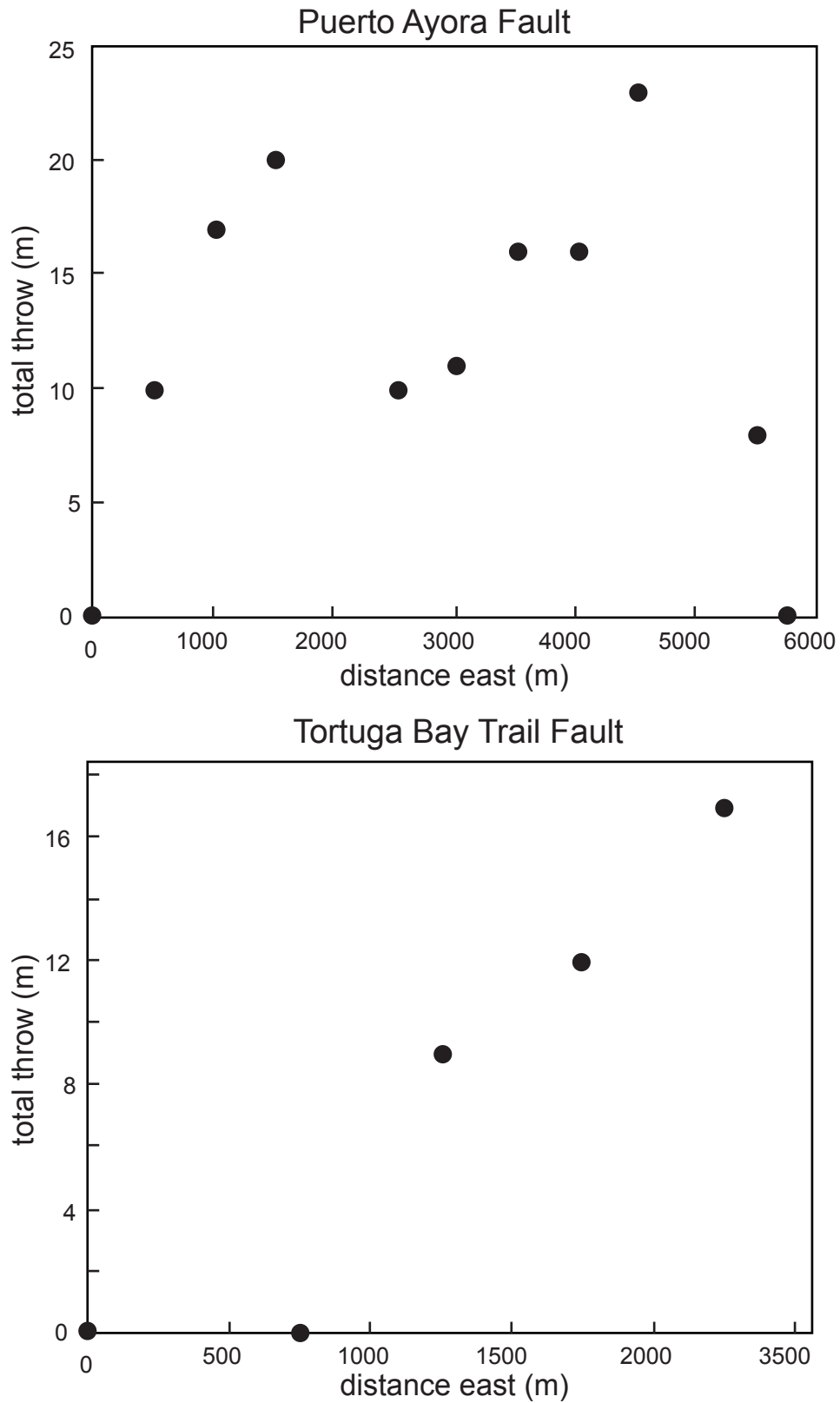
Table 1: Comparison of total fault throw measured using the DEM and the Trimble GPS systems.

Profile	DEM total throw			GPS fault throw			GPS total throw		
	max	min	throw	max	min	throw	max	min	throw
1	18.8	-22.2	41	16.5	-18.4	34.9	18.3	-21.1	39.4
2	15.0	-16.9	32	13.4	-10.8	24.2	13.4	-14.9	28.3
3	13.0	-18.0	31	6.5	-13.4	19.8	11.1	-13.4	24.4
4	13.4	-11.0	24	12.3	-8.9	21.2	12.3	-10.5	22.7
5	9.1	-7.8	17	6.4	-3.6	10	8.0	-6.1	14
6	9.4	-6.5	16	4.0	-3.0	7.1	4.7	-4.3	9
7	1.5	-1.2	3	0.6	-1.5	2	2.0	-1.5	3.5
8	6.4	-6.6	13	4.1	-3.8	7.9	5.8	-5.3	11.1

Table 2: $^{40}Ar/^{39}Ar$ data and ages. Samples marked with an '*' yielded plateau ages that were discordant with isochron ages and are considered unreliable.

Sample Name	Location		Elev. (m)	Plateau Age (ka)	± (2σ)	% ^{39}Ar	Isochron Age (ka)	± (2σ)	N	$^{40}Ar/^{36}Ar_i$	± (2σ)
	Deg. Lat.	Deg. Long.									
SC12-011	-0.73148	-90.31692	47	73.6	38	94.46	83.5	51	11	295.1	5.5
SC12-012*	-0.69863	-90.22364	0	699	80	67.44	594	143	9	296.7	1.5
SC12-015	-0.74286	-90.32467	41	257	112	95.03	320	171	15	294.4	3.4
SC12-020	-0.56739	-90.17453	36	1620	30	100	1620	40	20	296.4	2.8
SC12-024*	-0.5836	-90.1733	16	40.1	106	97.29	-250	112	19	297.4	1.7
SC12-027	-0.63759	-90.29519	416	208	14	73.61	242	35	8	292.3	3.2
SC12-038	-0.61789	-90.36569	623	125	31	93.5	69.3	42	14	300.5	3.4
SC12-040	-0.61715	-90.36520	603	271	17	81.29	282	54	9	294.5	4.7
SC12-046	-0.66620	-90.39413	388	151	17	95.3	180	45	12	289	9.8
SC12-059	-0.49388	-90.28613	28	1260	210	65.8	370	230	12	313.2	19.6
				1350	70	100	1270	70	20	300.3	2.2
SC12-060	-0.49394	-90.28582	30	1160	70	58.32	1470	630	6	290.1	11.8
SC12-067	-0.49090	-90.25342	48	1360	30	100	1370	40	17	295.2	1
SC12-070*	-0.51437	-90.29446	72	-3700	660	59.55	2780	2060	16	290.4	2.3
SC12-572B	-0.73636	-90.30458	38	416	36	97.88	386	76	12	296.7	2.7
SC12-584B*	-0.73856	-90.32131	31	900	600	24.51	-2210	3990	3	305.2	26.8

Fig. 8: Incremental heating summaries and inverse concordia diagrams for each ^{40}Ar/^{39}Ar analysis. Box heights on incremental heating diagrams are 2σ.

Fig. 8: (continued)
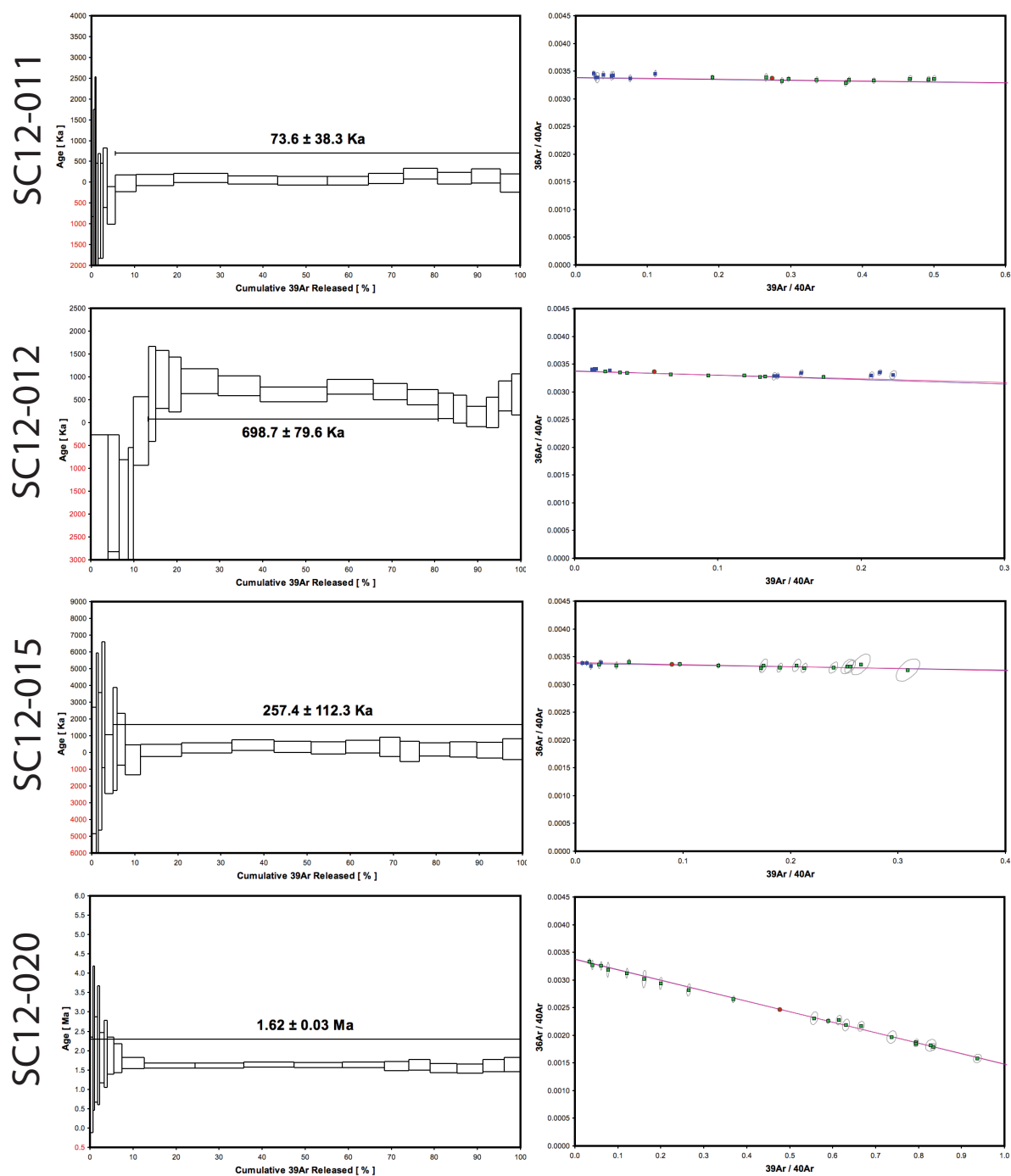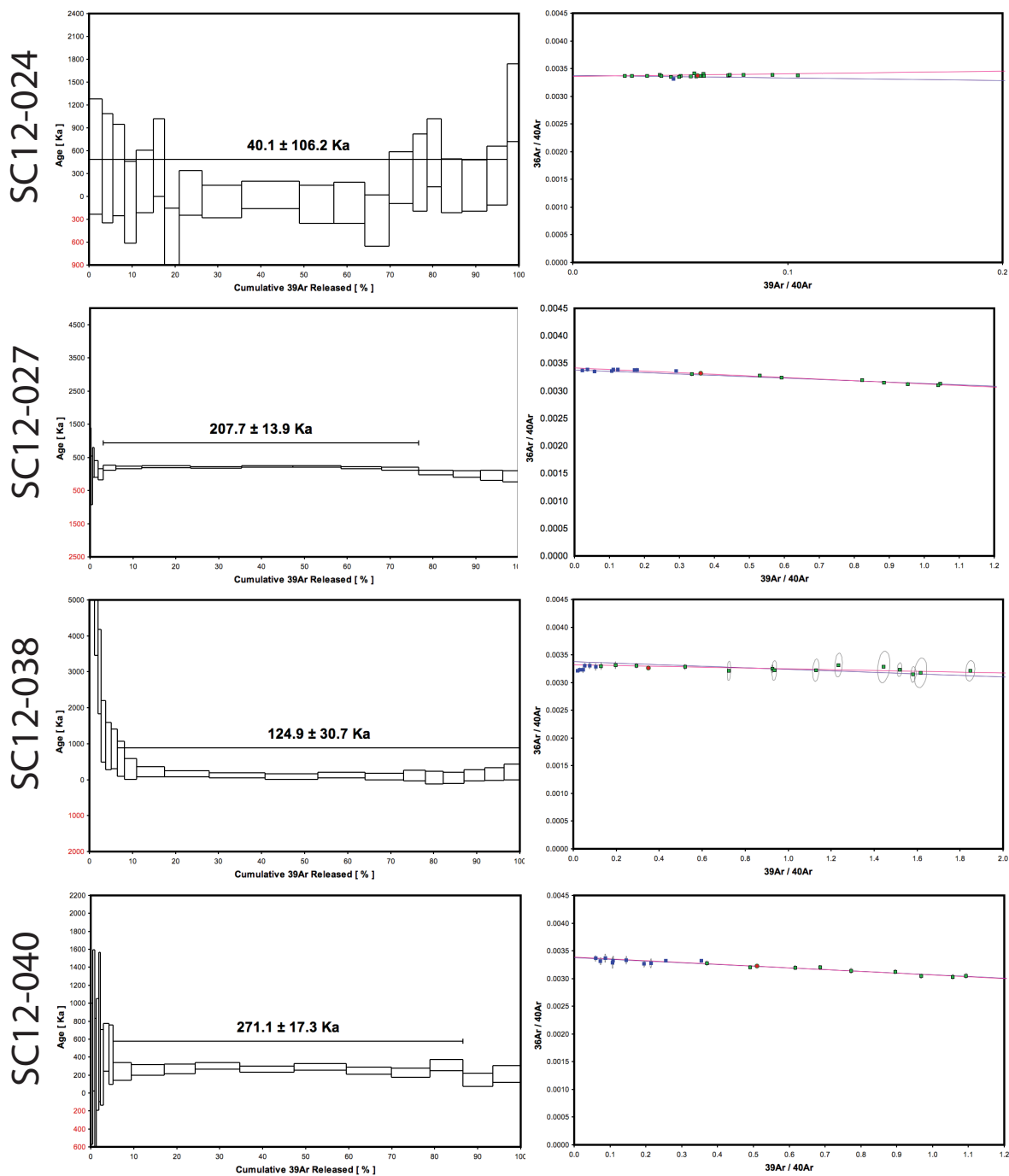
Fig. 8: (continued)

SC12-046   151.2 ± 16.8 Ka

SC12-0659   1.26 ± 0.21 Ma

SC12-059   1.35 ± 0.07 Ma

SC12-060   1.16 ± 0.07 Ma
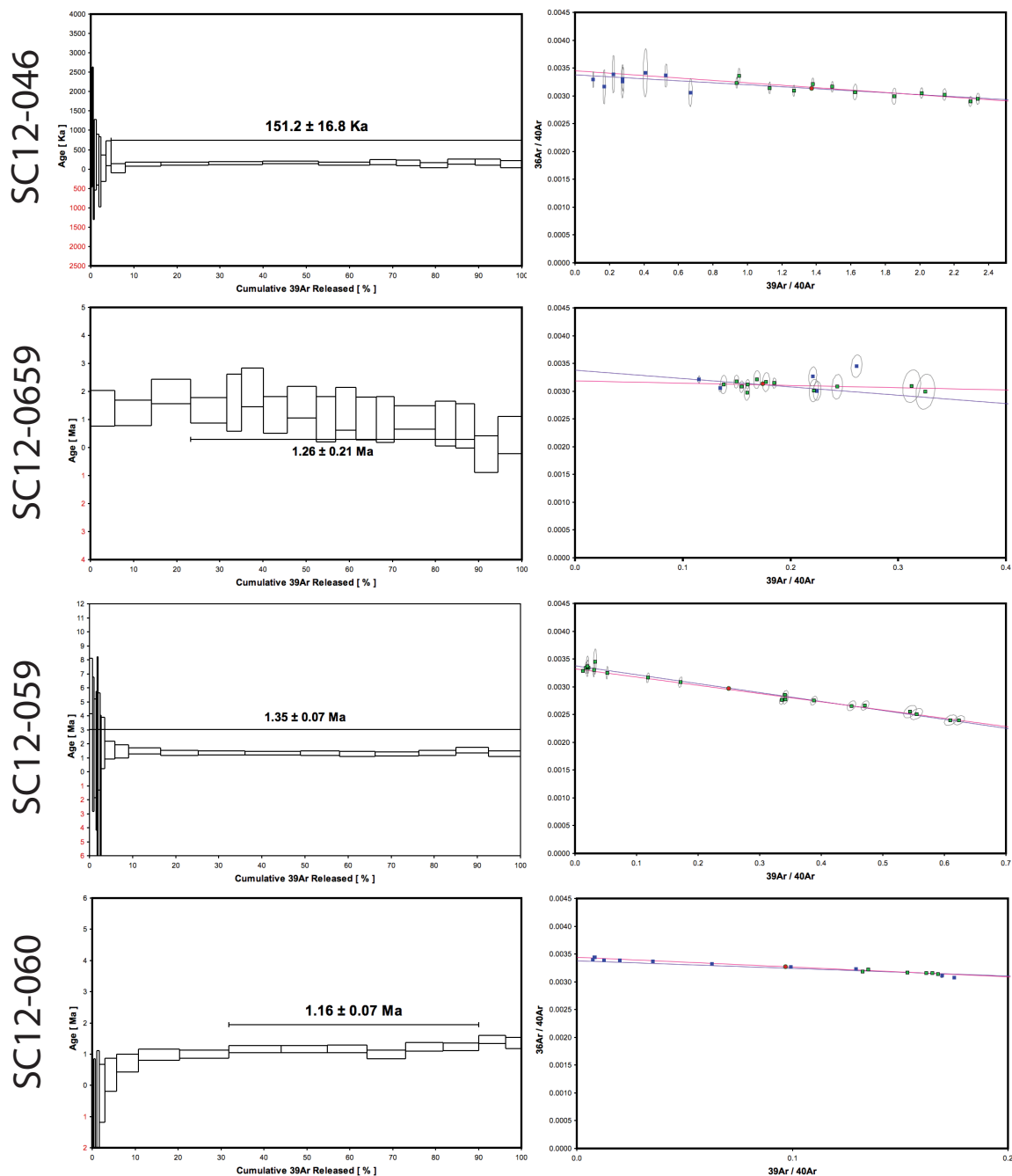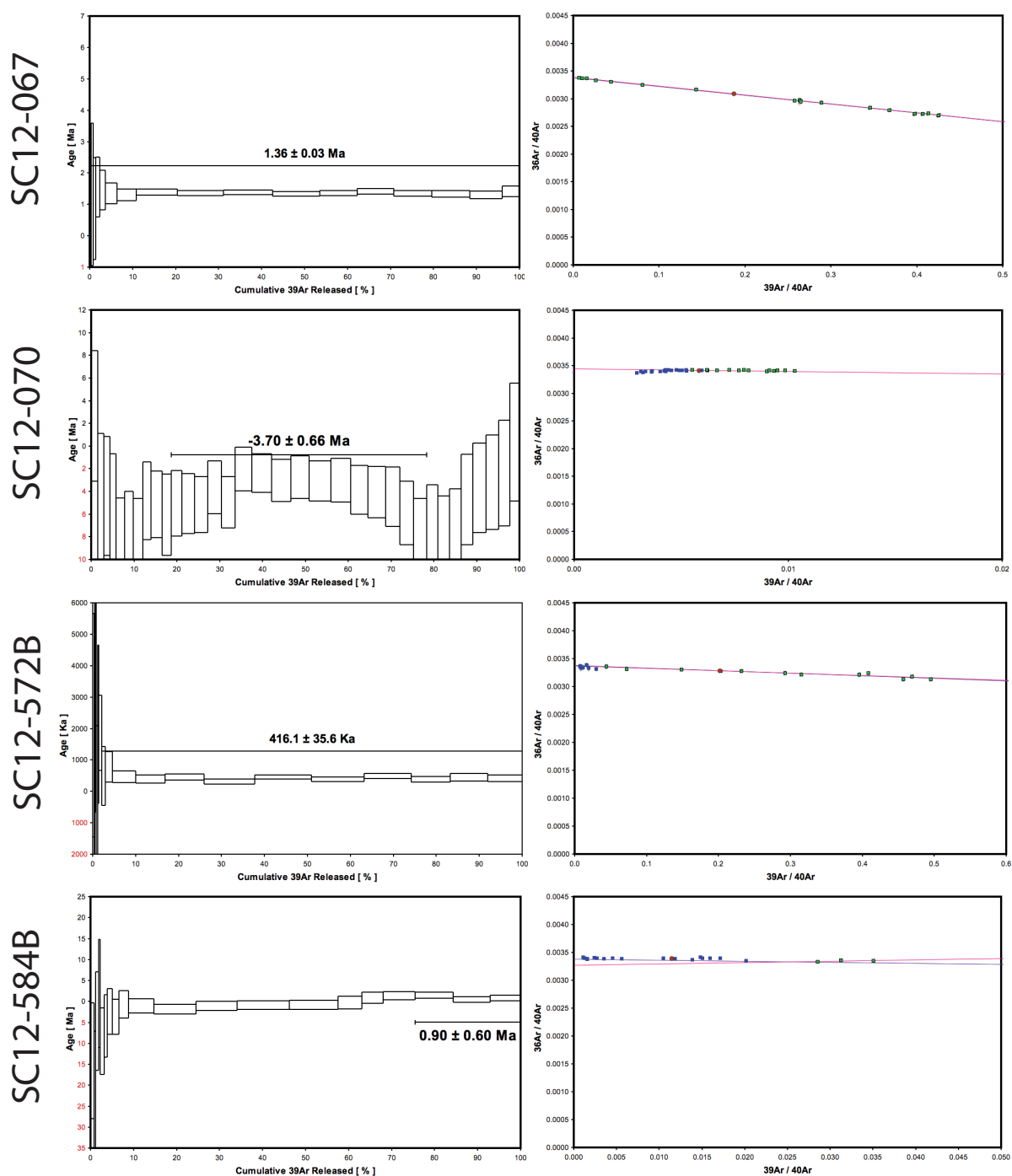
Fig. 8: (continued)

Fig. 9: Compilation of all geochronological analyses for Santa Cruz Island., including concordant analyses from this study Previous ages, compiled by Geist et al. (2014b) are plotted in grey (Kurz & Geist, 1999; White et al., 1993). New $^{40}Ar/^{39}Ar$ ages from this study are plotted as black boxes, and positioned where they overlap previous data on the x-axis.
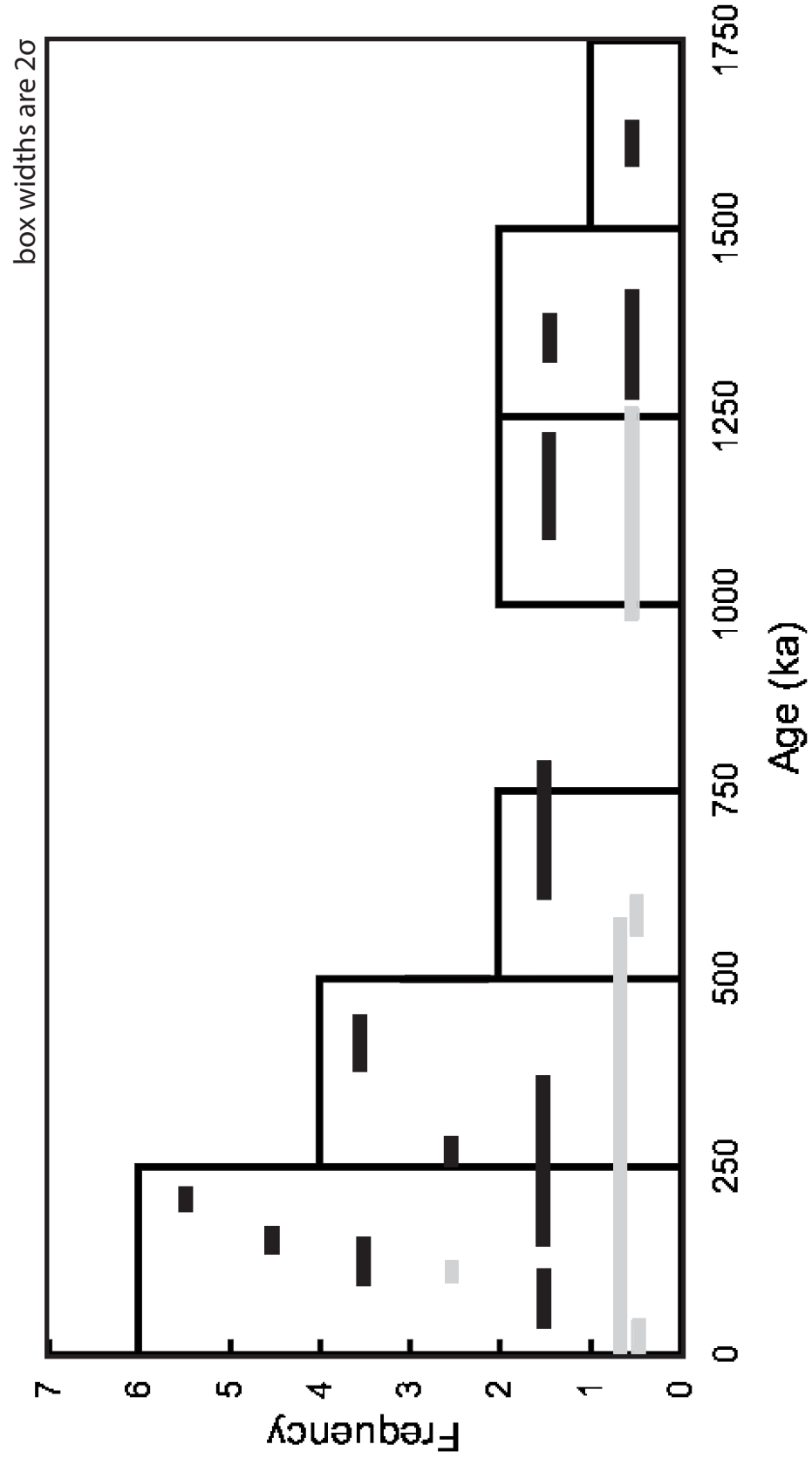
Table 3: Table of data used for calculating cosmogenic ^{3}He exposure ages.

Sample Name	Location		Elev.	^{4}He crush	^{3}He/^{4}He crush	±	Weight	^{4}He melt	±	^{3}He/^{4}He melt	±	Atoms ^{3}He	±
	Lat. Deg.	Long. Deg.	(m)	(ncc/gram)	(R/R$_a$)	(2σ)	(g)	(ncc/gram)	(2σ)	(R/R$_a$)	(2σ)	(X 10^6)	(2σ)
SC12-016-fb	-0.74324	-90.32423	25.8	0.662	7.6	0.6	0.1877	0.66	0.013	76.0	3.3	0.316	0.02
SC12-581	-0.73431	-90.30915	27.1	31.4	8.3	0.3	0.2973	31.39	0.63	9.1	0.3	0.291	0.18
SC12-582	-0.73267	-90.31267	24.0	52.2	8.1	0.3	0.2455	52.19	1.04	8.9	0.3	0.393	0.24
SC12-583	-0.73421	-90.30874	32.6	19.2	8.0	0.3	0.2888	19.16	0.38	9.9	0.4	0.399	0.11
SC12-583 -fb	-0.73421	-90.30874	32.6	60.3	8.3	0.3	0.1371	60.28	1.21	9.0	0.3	0.213	0.15
SC12-584A	-0.73858	-90.32126	20.6	1.30	8.1	0.4	0.2226	1.30	0.026	86.5	3.4	0.843	0.04
SC12-584A-fb	-0.73858	-90.32126	20.6	1.19	8.8	0.4	0.2414	1.19	0.024	92.1	3.6	0.892	0.04
SC12-584B	-0.73858	-90.32126	20.6	0.962	7.5	0.6	0.2227	0.96	0.019	87.9	3.5	0.641	0.03
SC12-584B-fb	-0.73858	-90.32126	20.6	1.39	7.0	0.8	0.2632	1.39	0.028	62.8	2.3	0.758	0.04
SC12-589	-0.74602	-90.28361	22.9	3.39	8.4	0.4	0.2900	3.39	0.068	53.8	2.0	1.660	0.08
SC12-606	-0.73129	-90.31958	49.5	0.782	7.9	0.8	0.3091	0.78	0.016	61.6	2.5	0.483	0.03
SC12-610	-0.74544	-90.32086	29.0	5.44	8.6	0.4	0.2018	5.44	0.109	20.4	0.8	0.481	0.04
SC12-611A-C	-0.74902	-90.34772	25.0	3.90	8.0	0.4	0.2571	3.90	0.078	11.9	0.5	0.145	0.03
SC12-611B	-0.74902	-90.34772	25.0	3.95	8.2	0.4	0.2205	3.95	0.079	37.4	1.4	0.948	0.05
SC12-614	-0.74324	-90.32423	25.8	0.593	6.3	0.8	0.1555	0.59	0.012	48.3	10.9	0.144	0.04

Table 4: Ages calculated from data summarized in Table 3. "Analytical" uncertainty column takes into account the analytical precision only, whereas the "prod. rate" uncertainty is the analytical and production rate uncertainties added in quadrature.

| Sample Name	Shielding	Age w/Shielding Corr. (ka)	Age w/o Shielding Corr. (ka)	± Analytical (2σ)	± Prod. Rate (2σ)
SC12-016-fb	0.6211	34	23	2	5
SC12-581	0.5047	27	14	17	17
SC12-582	0.4247	67	22	41	42
SC12-583	0.6457	31	19	9	10
SC12-583 -fb	0.6457	35	21	25	25
SC12-584A	0.6674	82	53	4	13
SC12-584A-fb	0.6674	80	52	4	13
SC12-584B	0.4668	78	40	4	12
SC12-584B-fb	0.4668	78	40	4	12
SC12-589	0.6221	115	80	6	18
SC12-606	0.4901	38	21	2	5
SC12-610	0.5468	48	33	4	8
SC12-611A-C	0.5066	16	8	3	4
SC12-611B	0.2458	247	60	14	38
SC12-614	0.0686	33	13	9	10

Fig. 10: Analytical reproducibility of $^{3}He_{c}$ analyses.
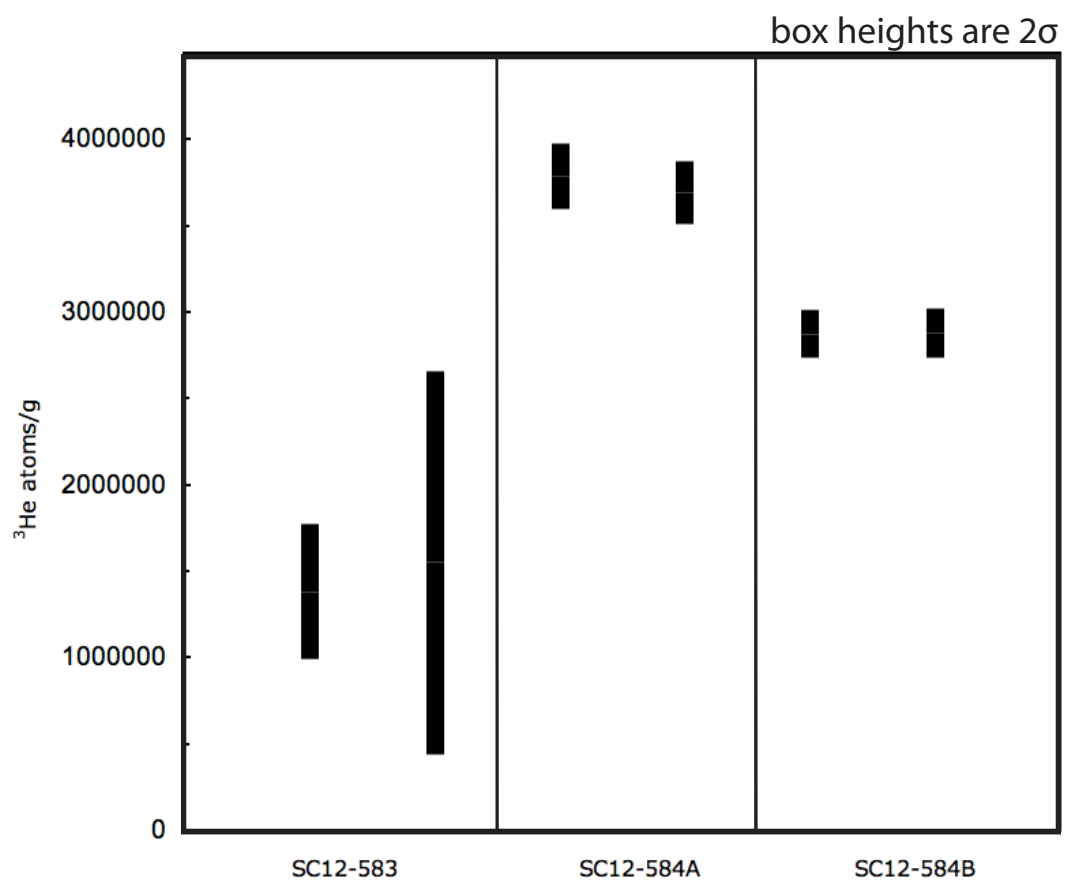
Fig. 11: Cosmogenic ^{3}He exposure ages for 12 samples collected from vertical fault scarps along four of the primary faults on the southern flank of Santa Cruz Island (Fig. 4A. Samples that were collected from the same fault are grouped together and arranged from west to east along strike of the fault they were collected (Fig 4A). The dark blue bars are ages corrected for topographic and geometric shielding; the size of the dark blue bars are the analytical uncertainty (2σ). Red bars are ages calculated with no topographic or geometric shielding correction; uncertainty on these bars is representative of only analytical uncertainty. Light blue bars are the same ages as the dark blue bars but include production rate uncertainty added in quadrature with analytical uncertainty. Where relevant, weighted mean ages are calculated for each fault and are shown as horizontal black bars, with 2σ uncertainty for the weighted mean age shown as a lighter grey box. The weighted mean age for the Puerto Ayora fault excludes SC12-589 (far right, see results for explanation).
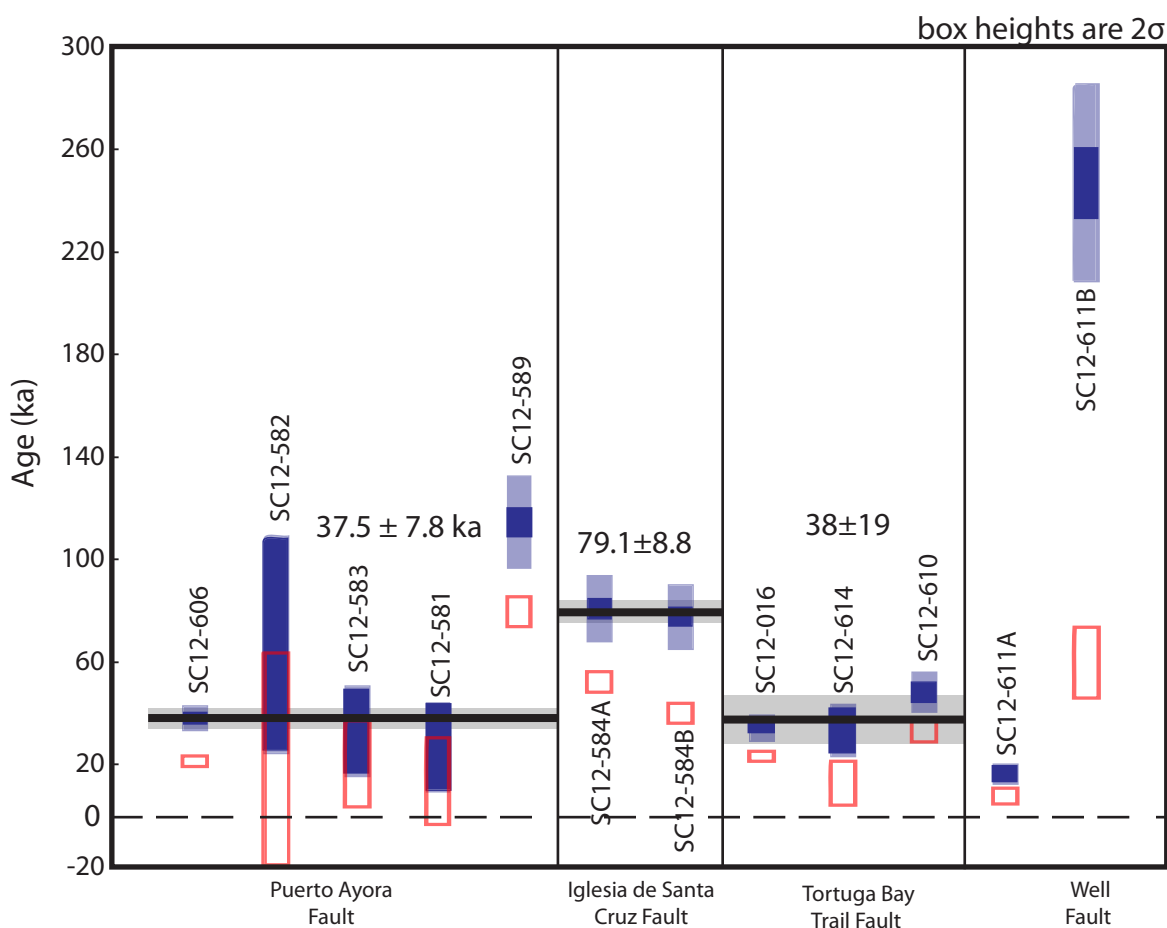
Table 5: Gravimeter measurements collected on Santa Cruz Island during 2012 gravity survey. FAA: Free Air Anomaly, BA: Bouguer Anomaly, calculated using a density of 2400 kg/m^3 of the volcanic topography.

Measurement	Location		Elev.	Time	Temperature	Voltage	Gravity	FAA	BA	Comment
	Deg. Lat	Deg. Long	(m)		(F)		(mGal)	(mGal)	(mGal)	
2	-0.64773	-90.41414	416.5	8:49:43	52.8	10.8	1673.76	1802.01	1.12	base
3	-0.64773	-90.41414	404.0	9:07:33	52.8	10.8	1677.29	1801.69	0.73	S. Rosa
4	-0.64337	-90.42014	410.0	9:17:07	52.7	10.8	1673.39	1799.65	-3.52	S. Rosa
5	-0.63870	-90.42752	417.9	9:26:38	52.7	10.8	1670.26	1798.97	-3.87	S. Rosa
6	-0.63331	-90.43457	366.2	9:36:20	52.7	10.5	1681.76	1794.53	-3.03	S. Rosa
7	-0.63246	-90.43568	362.9	9:42:52	52.7	10.8	1681.55	1793.31	-4.80	S. Rosa
8	-0.65323	-90.40535	416.5	9:59:40	52.7	10.8	1673.74	1802.00	-1.02	base
9	-0.69445	-90.32474	179.9	10:28:43	52.7	10.7	1725.41	1780.58	1.88	Garrapatero
10	-0.69431	-90.31860	202.3	10:38:32	52.7	10.4	1720.65	1782.73	1.88	Garrapatero
11	-0.69062	-90.31151	194.7	10:48:46	52.7	10.7	1722.47	1782.22	1.19	Garrapatero
12	-0.68593	-90.30469	219.0	10:58:10	52.7	10.7	1717.43	1784.69	1.31	Garrapatero
13	-0.68205	-90.29552	239.4	11:07:55	52.7	10.7	1713.17	1786.74	1.79	Garrapatero
14	-0.67826	-90.28791	236.9	11:16:24	52.7	10.7	1713.49	1786.30	1.34	Garrapatero
15	-0.67275	-90.27995	250.6	11:26:31	52.8	10.7	1709.59	1786.64	0.65	Garrapatero
16	-0.66935	-90.27315	272.5	11:34:56	52.8	10.7	1706.39	1790.21	1.93	Garrapatero
17	-0.66912	-90.26523	261.9	11:43:52	52.7	10.7	1705.98	1786.53	-0.68	Garrapatero
18	-0.66834	-90.25908	240.8	11:53:56	52.7	10.6	1712.61	1786.65	1.84	Garrapatero
19	-0.67019	-90.25149	199.3	12:02:01	52.8	10.6	1720.46	1781.70	0.45	Garrapatero
20	-0.67332	-90.24341	141.6	12:09:06	52.7	10.6	1733.11	1776.53	1.69	Garrapatero
21	-0.67582	-90.23660	102.2	12:16:21	52.7	10.6	1739.84	1771.10	-0.75	Garrapatero
22	-0.67760	-90.22934	64.9	12:25:09	52.7	10.6	1747.47	1767.22	0.56	Garrapatero
23	-0.68203	-90.22382	39.4	12:33:41	52.8	10.6	1751.92	1763.79	-0.19	Garrapatero
24	-0.68971	-90.22261	17.3	12:42:02	52.8	10.6	1757.81	1762.85	1.42	Garrapatero
25	-0.65328	-90.40534	416.5	13:47:36	52.8	10.5	1673.73	1802.05	-0.85	base
26	-0.64180	-90.40222	477.2	13:57:51	52.7	10.5	1659.72	1806.81	-6.34	Baltra
27	-0.63566	-90.39616	549.7	14:05:31	52.7	10.5	1645.78	1815.25	-1.48	Baltra
28	-0.62584	-90.38509	607.9	14:14:16	52.7	10.5	1632.66	1820.11	-1.95	Baltra
29	-0.61818	-90.37574	573.4	14:22:13	52.7	10.5	1641.35	1818.17	-1.06	Baltra
30	-0.60672	-90.36725	478.7	14:31:57	52.7	10.5	1662.53	1810.15	1.14	Baltra
31	-0.59744	-90.36030	405.1	14:39:45	52.7	10.5	1682.79	1807.72	7.82	Baltra
32	-0.58808	-90.35320	330.2	14:47:13	52.7	10.5	1694.67	1796.50	3.14	Baltra
33	-0.57871	-90.34611	298.1	14:55:38	52.7	10.5	1699.86	1791.81	1.35	Baltra
34	-0.56961	-90.33946	253.2	15:03:49	52.7	10.5	1707.90	1786.00	-0.03	Baltra
35	-0.56233	-90.33400	211.6	15:11:20	52.7	10.4	1715.58	1780.87	-0.39	Baltra
36	-0.55475	-90.32844	140.3	15:16:20	52.7	10.4	1730.32	1773.62	-0.22	Baltra
37	-0.54746	-90.32311	105.2	15:24:04	52.7	10.4	1738.07	1770.55	0.31	Baltra
38	-0.53854	-90.31653	80.8	15:32:10	52.7	10.3	1742.88	1767.84	0.04	Baltra
39	-0.52873	-90.30932	76.6	15:39:32	52.7	10.3	1742.89	1766.57	-0.68	Baltra
40	-0.51825	-90.30130	50.9	15:48:05	52.8	10.2	1747.87	1763.64	-0.52	Baltra

Table 5: (continued)

Measurement	Location		Elev.	Time	Temperature	Voltage	Gravity	FAA	BA	Comment
	Deg. Lat	Deg. Long	(m)		(F)		(mGal)	(mGal)	(mGal)	
41	-0.51048	-90.29535	50.1	15:54:31	52.7	10.2	1746.38	1761.92	-2.34	Baltra
42	-0.50382	-90.29085	27.3	16:02:03	52.7	10.1	1749.44	1757.95	-4.06	Baltra
43	-0.49359	-90.28597	8.3	16:09:20	52.7	10.0	1747.17	1749.84	-9.90	Baltra
44	-0.48767	-90.28004	-0.6	16:17:36	52.8	9.9	1749.62	1749.55	-9.94	Baltra
45	-0.65331	-90.40528	416.5	16:51:48	52.8	9.1	1673.61	1801.97	-0.93	base
46	-0.65340	-90.40534	416.5	8:31:47	52.8	11.5	1673.73	1802.01	-0.89	base
47	-0.66086	-90.39817	403.3	8:40:41	52.7	11.9	1676.50	1800.68	-1.73	P. Ayora
48	-0.66822	-90.39208	366.7	8:48:16	52.7	11.9	1684.70	1797.58	-1.07	P. Ayora
49	-0.67437	-90.38462	341.7	8:56:29	52.7	11.5	1689.96	1795.10	-0.41	P. Ayora
50	-0.67849	-90.37574	313.1	9:06:37	52.7	11.8	1698.91	1795.21	3.37	P. Ayora
51	-0.68412	-90.36788	276.0	9:15:04	52.7	11.8	1707.79	1792.63	4.86	P. Ayora
52	-0.68788	-90.36120	223.5	9:22:31	52.7	11.8	1716.14	1784.77	0.91	P. Ayora
53	-0.68794	-90.35176	226.2	9:29:43	52.7	11.8	1715.20	1784.67	0.37	P. Ayora
54	-0.68944	-90.34339	226.3	9:38:53	52.7	11.8	1714.76	1784.25	0.49	P. Ayora
55	-0.69338	-90.33486	179.6	9:49:59	52.7	11.7	1723.90	1778.96	-0.76	P. Ayora
56	-0.69444	-90.32566	178.8	10:01:55	52.7	11.7	1725.61	1780.42	1.60	P. Ayora
57	-0.70063	-90.32691	163.6	10:13:58	52.7	11.7	1728.67	1778.77	1.91	P. Ayora
58	-0.70870	-90.32569	140.1	10:22:25	52.7	11.7	1733.54	1776.37	1.97	P. Ayora
59	-0.71700	-90.32624	112.5	10:31:30	52.8	11.7	1738.97	1773.25	1.23	P. Ayora
60	-0.72605	-90.32750	71.4	10:41:10	52.7	11.7	1748.06	1769.64	2.05	P. Ayora
61	-0.73443	-90.32777	57.7	10:49:12	52.7	11.7	1751.05	1768.38	2.44	P. Ayora
62	-0.74041	-90.32233	16.4	10:57:52	52.7	11.7	1760.54	1765.11	3.33	P. Ayora
63	-0.74395	-90.31519	8.6	11:05:06	52.7	11.7	1761.91	1764.06	3.23	P. Ayora
64	-0.74331	-90.30471	-0.7	11:24:49	52.8	11.3	1763.40	1762.67	2.92	gravity tie
65	-0.65328	-90.40535	416.5	12:04:10	52.8	11.6	1673.80	1802.01	-0.89	base

Fig. 12: Free air anomaly from N-S and from E-W on Santa Cruz Island. Elevation is shown in green, and the FAA is in blue.
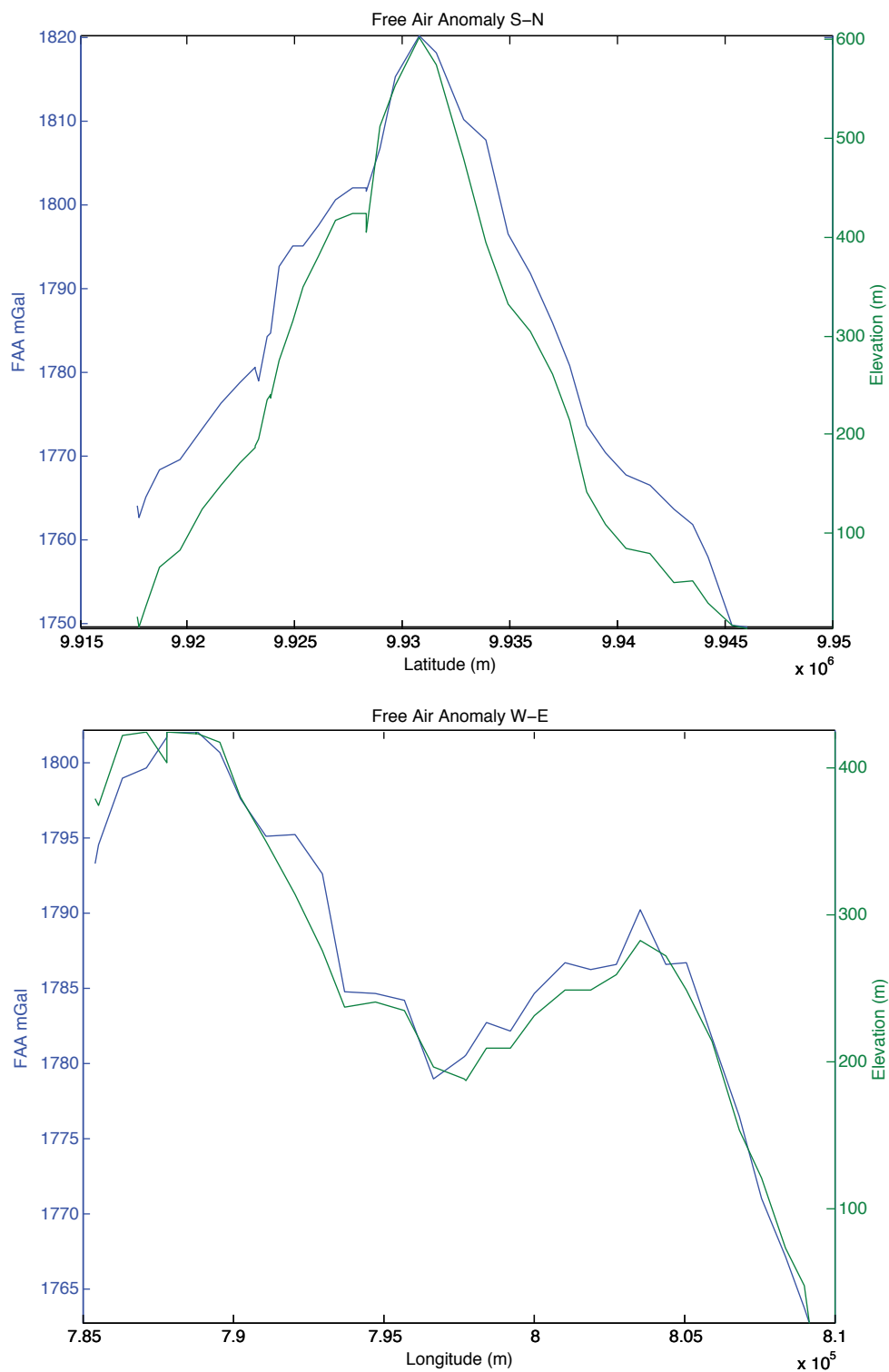
Fig. 13: Bouguer anomaly from N-S and from E-W on Santa Cruz Island. Elevation is shown in green, and BA is in blue
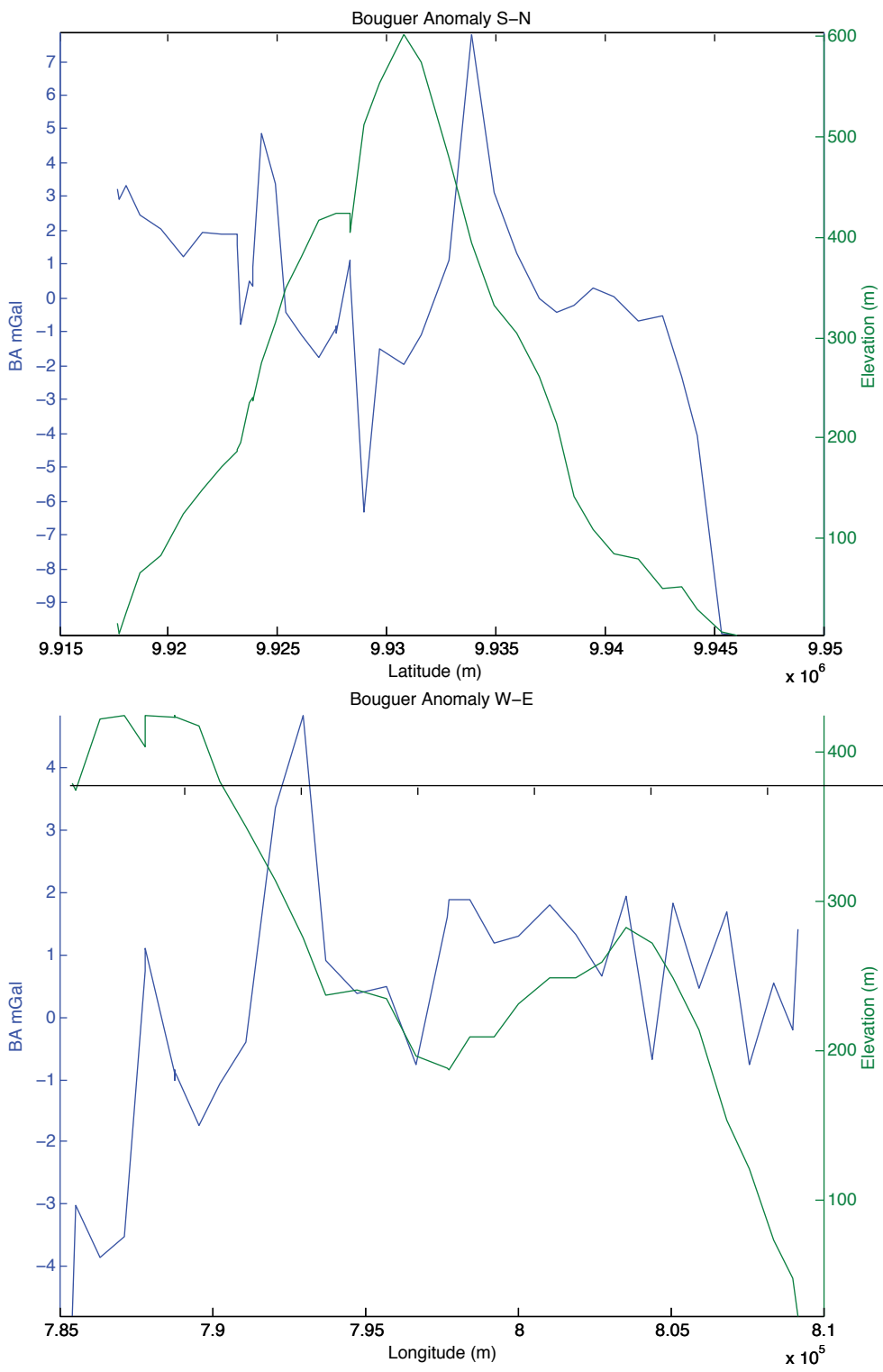
Fig. 14: Relationship between Bouguer anomaly (mGal) and elevation for E-W and N-S gravity transects using densities of 2000, 2200, 2400, 2600, 2800 kg/m^3 to calculate Bouguer anomaly. Linear regression is calculated for the resulting data, R-value indicating fit is shown within each graph title.
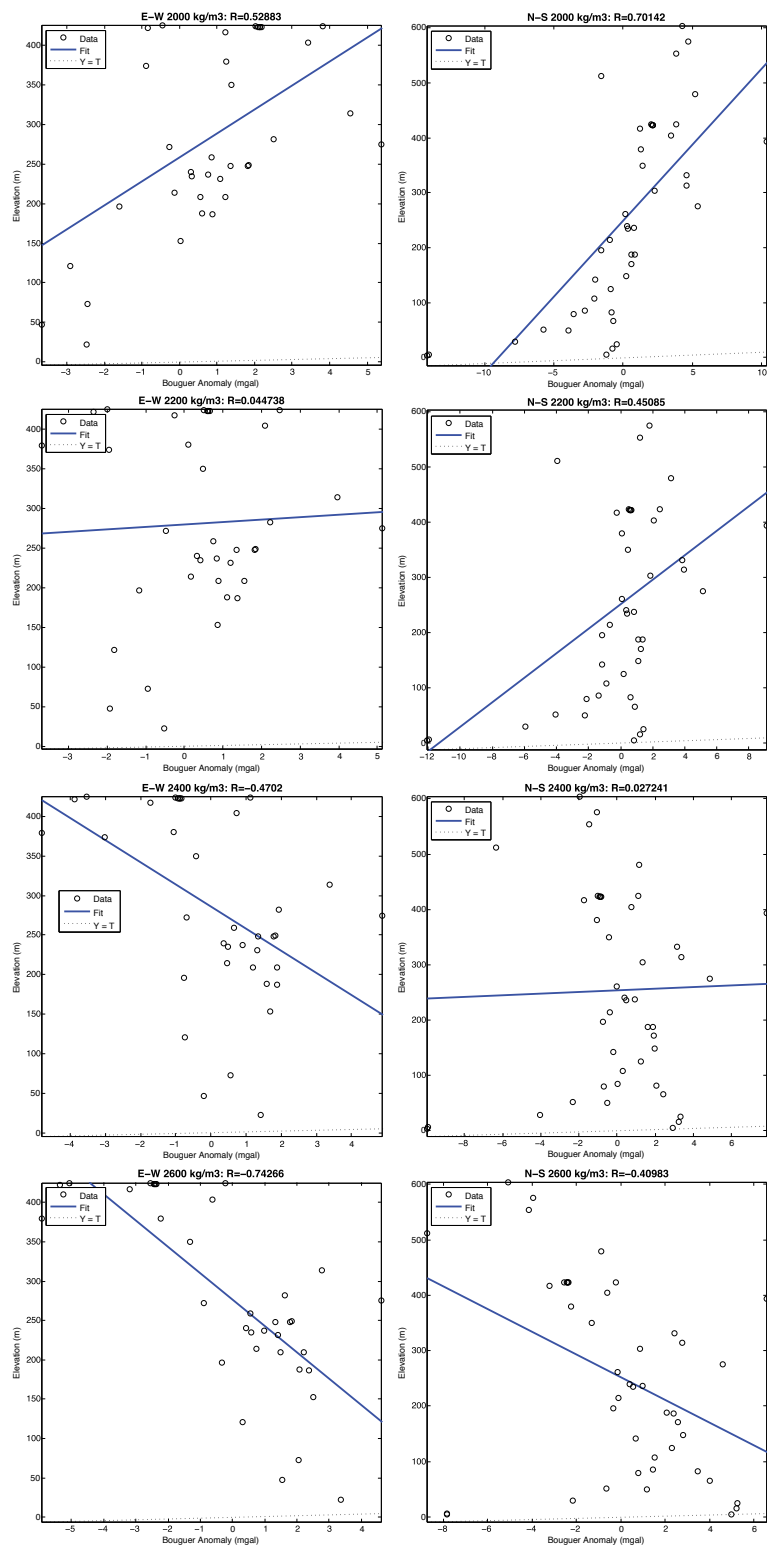
Fig. 15: Gravity inversion results for N-S and E-W transects for various specified parameters.
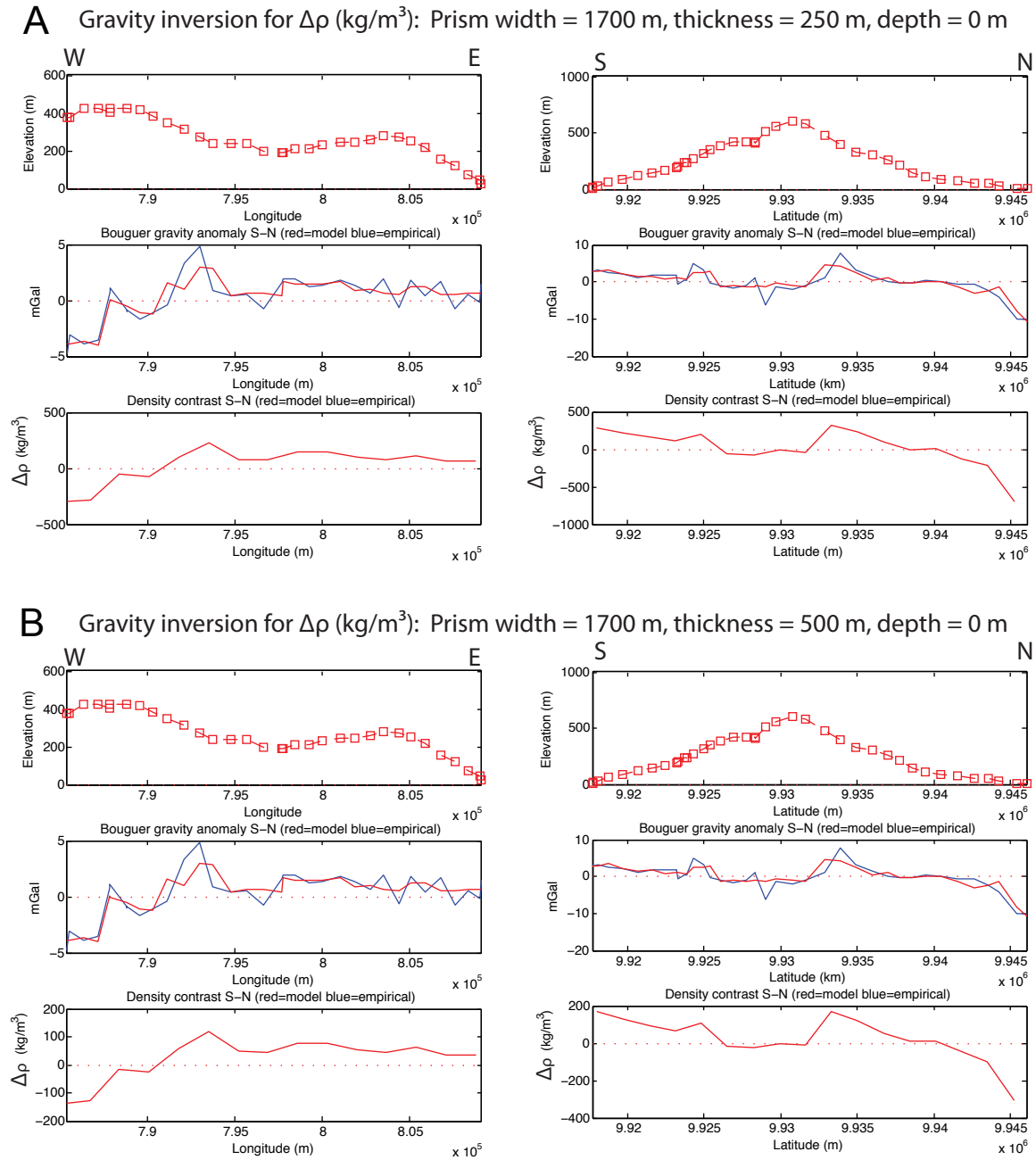
Fig. 15: (continued)

C Gravity inversion for Δρ (kg/m³): Prism width = 1700 m, thickness = 1000 m, depth = 0 m
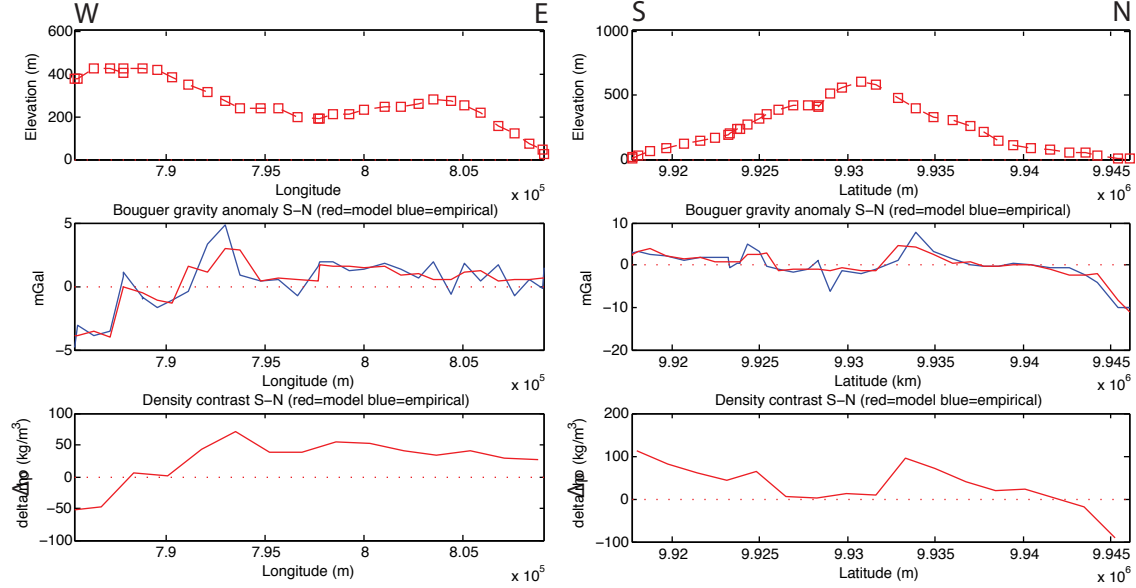
D Gravity inversion for Δρ (kg/m³): Prism width = 1700 m, thickness = 1500 m, depth = 0 m
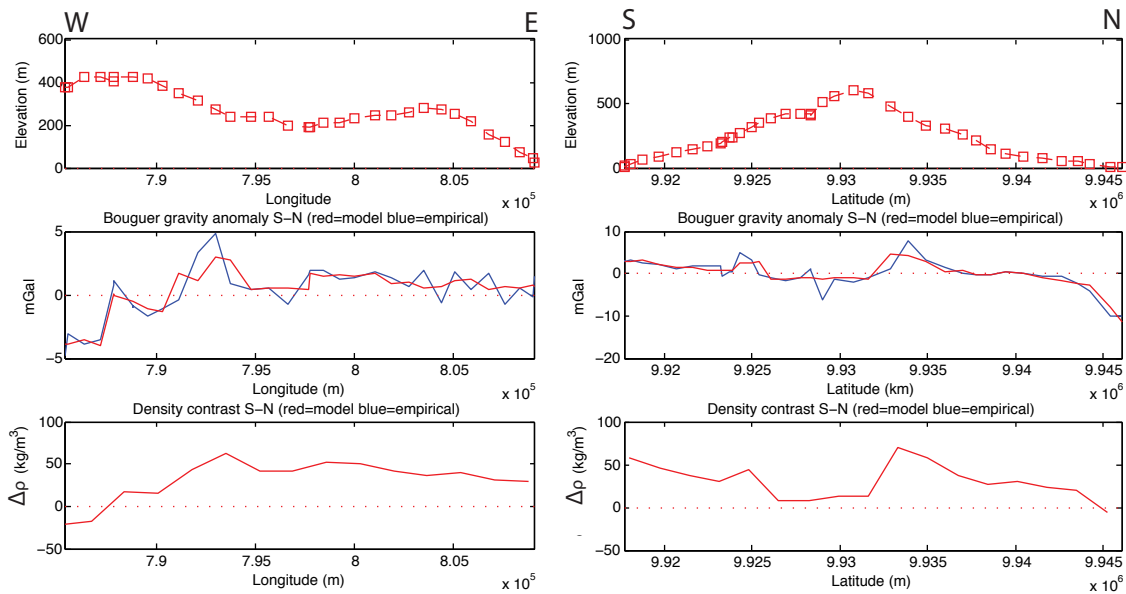
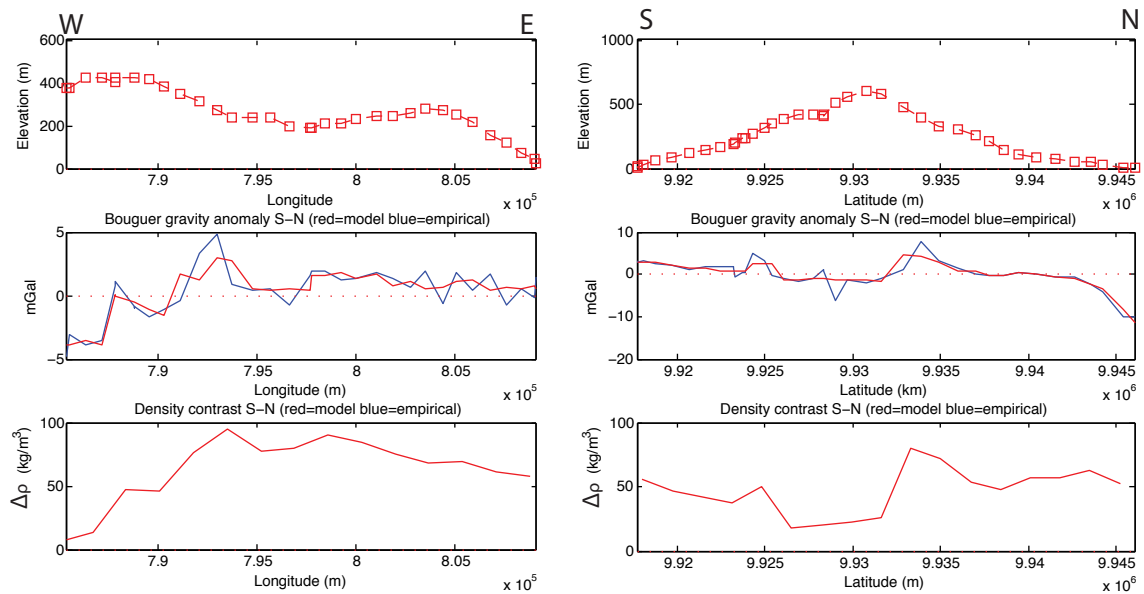Fig. 15: (continued)

E Gravity inversion for Δρ (kg/m³): Prism width = 1700 m, thickness = 500 m, depth = 500 m
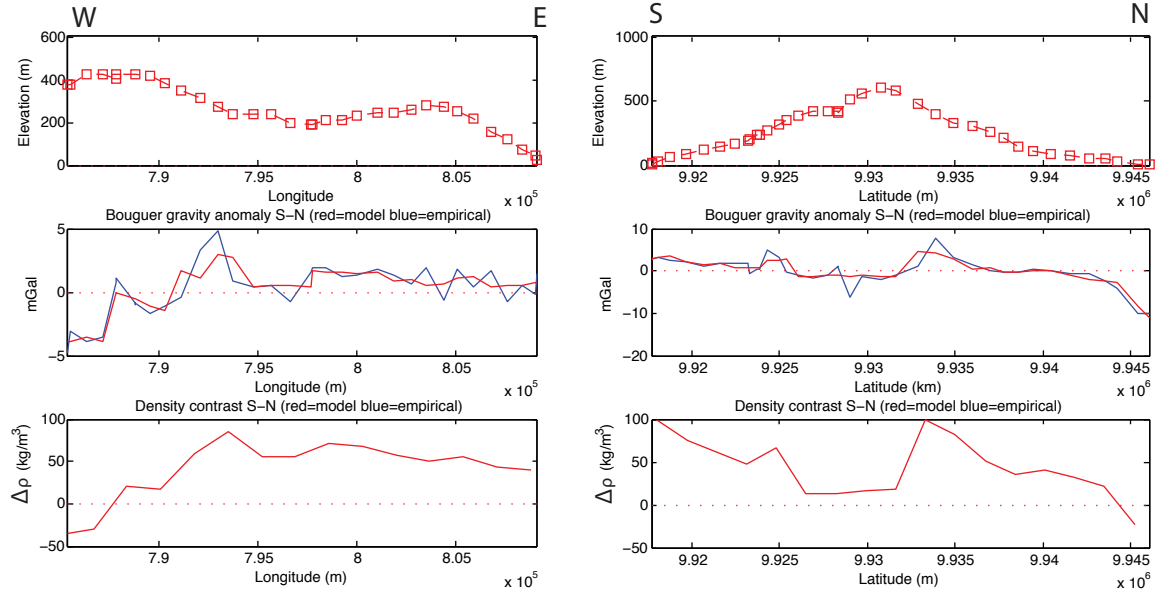
F Gravity inversion for Δρ (kg/m³): Prism width = 1700 m, thickness = 500 m, depth = 500 m

Fig. 16: Photo on the northeast flank of Santa Cruz, depicting a north-facing fault scarp part of the Northern Fault group.

Fig. 17: Photographs of sampling location for SC12-572B, along the N. Puerto Ayora Fault scarp. Photographs depict a lava flow that filled in >10 cm joints of underlying lava prior to the formation of the N. Puerto Ayora Fault. Sample SC12-572B was collected from the upper lava flow.
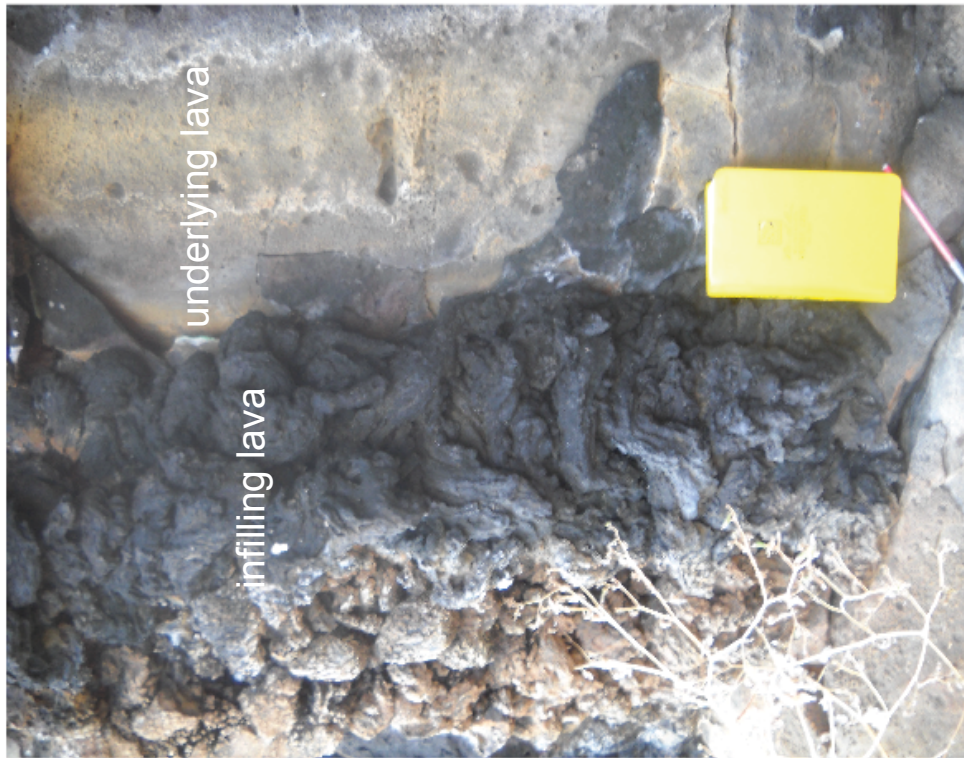
Fig. 18: Select isotopic and major element data plotted against the age for samples dated in this study. Chemistry data from Wilson (2013).
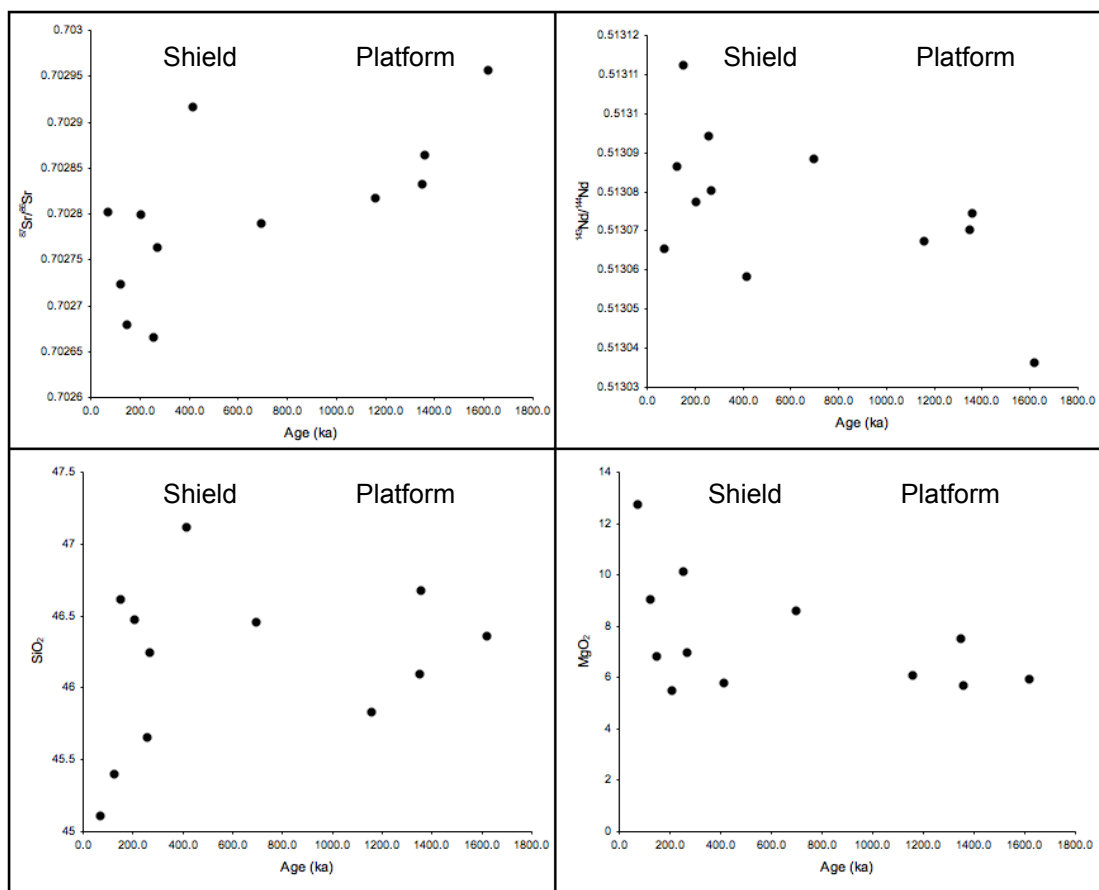
Fig. 19: Depth to top of melting column for the samples dated in this study. D_{top} is calculated using the methods of Gibson & Geist (2010).
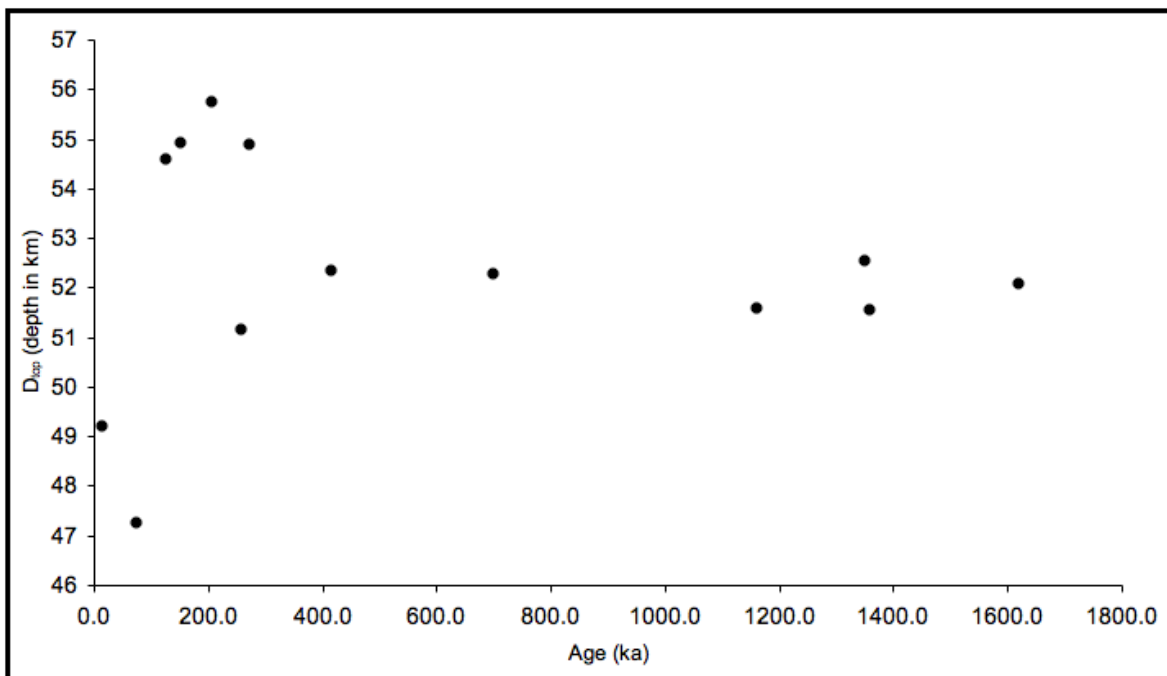
Fig. 20: Conceptual model illustrating the proposed stages of volcanism and deformation responsible for the variation of eastern and western Galápagos volcanoes. Vertical depths are drawn to scale. Depth of mantle solidus is approximated from Harpp et al. (2014). Time-distance scale calculated from Argus et al. (2010). Eruptive activity for each island is summarized from Swanson et al. (1974), White et al. (1993), Geist et al. (2014b), and this study. Descriptions of each stage of volcanism can be found in the discussion.